

1 The linkage between the warm Arctic and mid-latitude weather and climate is a hot topic for
2 cryosphere research community and for this reason, I see this study is interesting and worth to
3 be noticed as a scientific publication. The manuscript is well structured, and the objectives of
4 this study are clear. The content fits well the scope of ACP.

5 I recommend this manuscript to be published in ACP. However, I see there are some aspects
6 scientifically and technically that still need further improvement for better clarity of this
7 manuscript, I hope authors can make corresponding revisions based on my comments below:

8
9 1 Title: “Revisiting the trend in the occurrences of the “warm Arctic-cold Eurasian continent”
10 temperature pattern” Why “revisit”? Have you (authors) done this before? Or are there other
11 papers dealing with this matter before? if so, what are the scientific outcome from those
12 existing studies?

13 We have not carried out previous research on the potential mechanisms for the trends of
14 warm-Arctic-cold Eurasian per se, but there have been several other studies that are either
15 directly or indirectly related to this specific topic. Two main conclusions regarding the
16 forcing behind the trends stem from these studies. One conclusion is that the recent warm
17 Arctic-cold continents pattern can be attributable to the Arctic sea ice loss (Inoue et al., 2012;
18 Tang et al., 2013; Mori et al., 2014; Kug et al., 2015; Cohen et al., 2018; Mori et al., 2019);
19 The others disputed sea ice loss as a driver for the trend (Blackport et al., 2019; Fyfe, 2019),
20 Instead, they point to internal atmospheric variability and the Pacific and Atlantic SST
21 oscillations as potential forcing behind the trends (Lee et al., 2011; Sato et al., 2014;
22 Matsumura and Kosaka, 2019; Clark and Lee, 2019). Most of these previous studies and the
23 two school of thought were mentioned in the Introduction. Our work, which took a different
24 approach, confirmed the second school of thought. Because of these existing studies on this
25 topic, we used the word ‘revisiting’ in the title of our manuscript.

26
27 2 To my understanding, SOM is a pure advanced statistical tool and there is nothing related to
28 the physics, right? If this is the case, shall I say any results come from SOM have
29 uncertainties because you need to pre-define SOM nodes and this procedure is a kind
30 arbitrary, right? On top of it, as you pointed out in the abstract only 40% of the surface
31 temperature trends are explained by SOM pre-defined nodes that fit to your pre-condition, i.e.
32 warm Arctic-cold Eurasian continent. What I am trying to say is that for what kind of criteria
33 you need to be satisfied before you can make a rebuts conclusion to say: “ok, there is a
34 linkage” or “no, there isn’t a linkage”. This comment and “a kind of arbitrary” above come
35 from your description on line 141-143.

36 SOM is an advanced statistical tool for pattern extraction. Although SOM is superior to some
37 other existing pattern extraction tools such as EOF, it suffers from the same limitations as
38 other statistical tools in identifying physical modes. That was why a large part of the
39 manuscript was devoted to explain the existence of the patterns and their trends based on
40 physical understanding of atmosphere and ocean dynamics that had been established from
41 theoretical framework and/or from coupled ocean-atmosphere modeling. Yes, to use the SOM
42 method, one has to pre-define SOM nodes and the procedure is not completely objective. A
43 small grid (each node has larger frequency of occurrence) tends to miss transitions between
44 the main patterns that are retained by a large grid. But an excessively large grid could

45 sidetrack the attention from the main variability patterns. Nevertheless, changing the grid
46 from 3x3 to 4x4 or even larger would not change the main conclusion.

47

48 3 How sensitivity of the data source will impact the final result? In this study, you have
49 applied ERA-Interim data. if you use other data resource, e.g. NCEP or MERRA, would be
50 your conclusion changed entirely or partly? I am not asking to use these data sets to rerun
51 SOM, but it would be nice to comment it at the end of this study.

52 We believe our results are not particularly sensitive to the specific large-scale reanalysis data
53 source. We could have also used ERA5, or NCEP or MERRA and arrived at similar
54 conclusions, although there might be some minor differences. We have added some
55 comments on this point at the end of the study.

56

57 4 Authors focused on the impacts of the SST anomalies over North Pacific and Atlantic
58 Oceans on the trend in the occurrences of the “warm Arctic cold Eurasian continent”
59 temperature pattern. The influence of decreasing Arctic sea ice cannot be ignored.

60 You may consider to add discussions on the influence of sea ice to your pre-defined warm
61 Arctic and cold Eurasian content.

62 We added some discussions on the influence of sea ice in the Conclusions and Discussions
63 section.

64

65 There are a number of technical details need to be clarified:

66 a) Fig.1: All “percent” sum together is larger than 100%, please check.

67 Changed

68

69 b) Fig.2: The color bar refers to what? Contour color? what are the background (fingerprint
70 like) information in each sub-plot? The text explanation for figure 2 (line 182 -185) and figure
71 2 presentation seems not match to each other. I suggest you remove unnecessary from the plot
72 and only show what you have explained in the text so readers can understand better.

73 Both color bar and contour color refer to 500-hPa geopotential height anomalies. Dotted
74 regions in each sub-plot indicate the above 95% confidence level.

75 We revised some of the discussion.

76

77 c) The comment above applied to at least Fig, 3, 4, 5 and 6.

78 In Figure 3-6, shaded and dotted regions indicate the above 95% confidence level.

79

80 d) “same as Figure2, but for,,,” This is not a good figure caption, please write clear with full
81 information. For those surface fluxes, I think you need to explain the unit of the fluxes, are
82 those daily accumulated fluxes?

83 We revised figure caption with details. The fluxes are daily accumulated fluxes, which are
84 now explained in the caption and text.

85

86 e) The sea ice concentration figure needs more explanations, e.g. node information was
87 missing; what was meant for positive and negative anomalous? is this also for winter season?
88 how about summer season? Now I realized you actually only investigate winter season for

89 everything, if so, you need to say this explicitly in the beginning of the paper.
90 We added node information. The anomalous sea ice concentration is a composite result based
91 on the occurrences of nodes. For example, the negative sea ice concentration corresponds to
92 the spatial pattern of air temperature for node 1. In this paper, we only examine warm
93 Arctic-cold continents pattern in boreal winter, which was mentioned in the first and second
94 paragraph of the manuscript.
95
96 f) Fig.7 and 14: I have difficult to understand these figures? What we can learn from those
97 figures? If you only tell the integrated total number of days for each node and compared with
98 showing this figure, what we will missing up?
99 Figure 7 and 14 show the integrated total number of days for each node. In Figure 7 and 14,
100 the numbers for nodes 1 and 4 are larger after 2000 than those prior to 2000. The opposite
101 occurs for nodes 6 and 9. Figure 14 mainly show an interdecadal variability of the number.
102 The trends in the number for nodes 1, 4, 6, and 9 are a fragment of the interdecadal variability.
103 We added clarification in the discussion.
104
105 g) Fig. 12: “wave activity flux”: This need to be explained more in detail both here and in the
106 text. 100m²/s, what is this? and in the caption:107 m²/s.
107 “vector 100m²/s” in the figure is figure legend of wave activity flux. The unit of stream
108 function is m²/s and its magnitude is the product of the values in the figure and 10⁷. We have
109 added explanation of wave activity flux in the discussion and in the figure caption with a
110 reference.
111
112 h) Please mark the study area in corresponding figures 2-6, to help readers understand the
113 mechanism impact more intuitively.
114 Marked
115
116 i) Table 3 is not mentioned in the article, and some problems of uppercase and lowercase
117 letters (such as not show or Not show), please check them carefully.
118 Changed
119
120 j) The order of the nodes should be consistent in figures, 10-12.
121 Changed
122
123 k) Authors should increase some discussions about the application of statistical results in
124 prediction of surface temperature Arctic cold Eurasian continent.
125 Added discussion
126
127 The results in this study are based on statistical analysis. Some numerical experiments may be
128 considered in the further studies.
129 Added
130
131

132 **Revisiting the trend in the occurrences of the “warm Arctic-cold Eurasian continent”**

133 **temperature pattern**

134 Lejiang Yu^{1,2*}, Shiyuan Zhong³, Cuijuan Sui⁴, and Bo Sun¹

135 1MNR Key Laboratory for Polar Science, Polar Research Institute of China, Shanghai, China

136 2 Southern Marine Science and Engineering Guangdong Laboratory (Zhuhai), Zhuhai, Guangdong,

137 China

138 3Department of Geography, Environment and Spatial Sciences, Michigan State University, East

139 Lansing, MI, USA

140 4 National Marine Environmental Forecasting Center, Beijing, China

141

142 *Corresponding Author’s address

143 Dr. Lejiang Yu

144 MNR Key Laboratory for Polar Science, Polar Research Institute of China

145 451 Jinqiao Rd. Shanghai, 200136

146 Phone: 86-21-58712034,

147 Email: yulejiang@sina.com.cn

148

149

150

151

152

153

154 **Abstract.** The recent increasing trend of “warm Arctic, cold continents” has attracted much attention,
155 but it remains debatable as to what forces are behind this phenomenon. Here, we revisited
156 surface-temperature variability over the Arctic and Eurasian continent by applying the
157 Self-Organizing-Map (SOM) technique to gridded daily surface temperature data. Nearly 40% of the
158 surface temperature trends are explained by the nine SOM patterns that depict the switch to the current
159 warm Arctic-cold Eurasia pattern at the beginning of this century from the reversed pattern that
160 dominated the 1980s and the 90s. Further, no cause-effect relationship is found between the Arctic
161 sea-ice loss and the cold spells in high-mid latitude Eurasian continent suggested by earlier studies.
162 Instead, the increasing trend in warm Arctic-cold Eurasia pattern appears to be related to the anomalous
163 atmospheric circulations associated with two Rossby wavetrains triggered by rising sea surface
164 temperature (SST) over the central North Pacific and the North Atlantic Oceans. On interdecadal
165 timescale, the recent increase in the occurrences of the warm Arctic-cold Eurasia pattern is a fragment
166 of the interdecadal variability of SST over the Atlantic Ocean as represented by the Atlantic
167 Multidecadal Oscillations (AMO), and over the central Pacific Ocean.

168

169 **Key words:** Warm Arctic-cold Eurasian continent, Arctic Sea ice, the Kara-Barents Sea, the
170 Self-Organizing-Map (SOM), the Pacific Decadal Oscillation (PDO), the Atlantic Multidecadal
171 Oscillation (AMO)

172

173

174

175

176 **1 Introduction**

177 In recent decades, winter season temperature in the Arctic has been rising at a rate faster than the
178 warming experienced in any other regions of the world (Stroeve et al., 2007; Screen and Simmonds,
179 2010; Stroeve, 2012). In contrasts, there has been an increasing trend in colder than normal winters
180 over the northern mid-latitude continents (Mori et al., 2014; [Cohen et al., 2014; 2018](#)). This pattern of
181 opposite winter temperature trend between the Arctic and high-mid latitude continents, referred to as
182 the warm Arctic-cold continents pattern (Overland et al., 2011; Cohen et al., 2014; Walsh, 2014), has
183 ~~also been observed on the interannual timescale~~[received considerable interest in the scientific](#)
184 [community especially with regard to dynamical and physical mechanisms for the development of the](#)
185 [phenomenon](#) (Mori et al., 2014; ~~Kug et al., 2015~~)~~The question as to what processes are responsible for~~
186 ~~the opposite change of winter air temperature between the Arctic and mid latitudes remain open~~
187 (~~Vihma, 2014; Barnes and Screen, 2015; Kug et al., 2015; Overland et al., 2015; Chen et al., 2018~~).

188 [Using observational analyses or coupled ocean-atmosphere modeling](#), ~~A~~ number of studies have
189 attributed the recent warm Arctic-cold continents pattern to the Arctic sea ice loss [in boreal winter](#)
190 (Inoue et al., 2012; Tang et al., 2013; Mori et al., 2014; Kug et al., 2015; Cohen et al., 2018; Mori et al.,
191 2019). Sea ice variability in different parts of the Arctic Ocean has been linked to climate variability in
192 different parts of the world. Specifically, sea ice loss in the Barents and Kara Seas has been linked to
193 cold winters over East Asia (~~add a reference~~ [Kim et al., 2014; Mori et al., 2014; Kug et al., 2015;](#)
194 [Overland et al., 2015](#)) [and in central Eurasia \(Mori et al., 2014\)](#), while a similar connection has been
195 found between cold winters in North America and sea ice retreat in the East Siberian and Chukchi Seas
196 (Kug et al., 2015). A most recent study (Matsumura and Kosaka, 2019) attributed the warm Arctic-cold
197 continents pattern to the combined effect of Arctic sea ice loss and the atmospheric teleconnection

198 induced by tropical Atlantic sea-surface temperature (SST) anomalies. ~~Some recent studies have~~
199 ~~suggested that the mid-latitude atmospheric circulation anomalies play a role in the formation of the~~
200 ~~warm Arctic-cold continents pattern (Luo et al., 2016; Peings et al., 2019).~~

201 Other studies, however, found no cause-and-effect relationship between Arctic sea ice loss and
202 mid-latitude climate anomalies (Blackport et al., 2019; Fyfe, 2019). Numerical modeling studies using
203 coupled ocean and atmospheric models simulated no cold mid-latitude winters when the models were
204 forced with reduced Arctic sea ice cover (McCusker et al., 2016; Sun et al., 2016; Koenig et al., 2019;
205 Blackport et al., 2019; Fyfe, 2019). ~~Instead, The results from~~ these studies pointed to internal
206 atmospheric variability as the likely cause for cold winters in mid-latitudes. Some studies have also
207 suggested that on the interannual timescale mid-latitude atmospheric circulation anomalies triggered by
208 the Pacific and Atlantic SST oscillations may explain both the Arctic sea ice loss and the cooling of the
209 high-mid latitudes (Lee et al., 2011; [Luo et al., 2016](#); [Peings et al., 2019](#); Matsumura and Kosaka, 2019;
210 Clark and Lee, 2019). The [sea surface temperature anomalies over the](#) Gulf Stream ~~have~~ ~~has~~ also been
211 linked to the Barents Sea ice loss and Eurasian cooling (Sato et al., 2014).

212 Despite the recent attention given to the warm Arctic-cold continents pattern, it remains debatable
213 as to ~~what the roles of various dynamical and physical processes play may be responsible in the~~
214 ~~formation of~~ ~~-for~~ this phenomenon. In this study, we revisit surface temperature variability over the
215 Arctic and Eurasia continent (40-90°N, 20-130°E), where the warm Arctic-cold continents pattern is a
216 prominent feature (Cohen et al., 2014; Mori et al., 2014), by applying the Self-Organizing-Map (SOM)
217 technique to daily surface temperature over the recent four decades. We will show that while the warm
218 Arctic-cold Eurasian continent pattern has dominated the recent two decades, its opposite pattern, cold
219 Arctic-warm Eurasia continent, appeared frequently in the 1980s and the 90s. Using century-long data,

220 we will further show that the warm Arctic-cold Eurasian continent pattern is an intrinsic climate mode
221 and the recent increasing trend in its occurrence is a reflection of an interdecadal variability of the
222 pattern. Using [linear regression](#)~~-method~~, we explain the reason for the recent increasing occurrences of
223 the warm Arctic-cold continents pattern. We also assess the role of the SST anomalies over the North
224 Pacific and Atlantic Oceans in the variability of the warm Arctic-cold Eurasia pattern on the
225 interdecadal time scale.

226 2 Datasets and methods

~~227 From the perspective of nonlinear dynamic, a region's climate has its intrinsic modes of variability, but
228 the frequency of occurrence of these internal modes can be modulated by remote forces external to the
229 region (Palmer, 1999; Hoskins and Woollings, 2015; Shepherd, 2016). In this study we will first obtain
230 the main modes of variability of wintertime surface temperature in a region (40-90 N, 20-130 E) by
231 applying the SOM method (Kohonen, 2001) to daily surface temperature data for the 40 winters in the
232 1979-2019 period. The use of daily data over four decades allows for capturing the variability across
233 two time scales (synoptic and decadal). We will then determine, through regression and composite
234 analyses, the relationships of these modes of climate variability of surface air temperature to known
235 climate variability modes at corresponding time scales.—~~

236 2.1 Datasets

237 Daily surface air temperature and other climate variables used in the current analyses, including
238 500 hPa geopotential height, 800-hPa wind and mean sea level pressure, all come from the [European
239 Centre for Medium-Range Weather Forecasts ~~Re-Analysis~~ \(ERA\)](#), the interim version (ERA-Interim;
240 Dee et al., 2011) [with a horizontal resolution of approximately 79 km \(T255\) and 60 vertical levels in
241 the atmosphere](#). Compared to the earlier versions of ERA (e.g., ERA-40, Uppala et al., 2005) and other

242 global re-analysis products (e.g. the NCEP reanalysis, Kalnay et al., 1996), ERA-Interim has been
243 found to be more accurate in portraying the Arctic warming trend (Dee et al., 2011; Screen and
244 Simmonds, 2011) despite its known warm and moist bias in the surface layer (Jakobson et al., 2012).

245 Daily sea ice data are obtained from the U.S. National Snow and Ice data Center
246 (ftp://sidacs.colorado.edu/DATASETS/nsidc0051_gsfc_nasateam_seaice/final-gsfc/north/daily).

247 Gridded monthly SST data used in the current analysis are obtained from the U.S. National Oceanic
248 and Atmospheric Administration (NOAA) data archives
249 (<ftp://ftp.cdc.noaa.gov/Datasets/noaa.oisst.v2.highres/>) (Reynolds et al. 2007).

250 The results obtained from the data within the recent four decades are put into the context of the
251 variability over longer time scales using data from the Twentieth Century Reanalysis project, version
252 2Ce (20CR) that spans more than a century from 1851 through 2015 (Compo et al., 2011). The 20CR
253 reanalysis data, which has a horizontal resolution of 2 °latitude by 2 °longitude and temporal resolution
254 of 6 hours. ~~Through the assimilation of surface observational pressure data, the 20CR reanalysis~~ was
255 produced by ~~the~~ model ~~whose driven at the~~ lower boundary ~~by condition is derived from observed~~
256 monthly SST and sea ice conditions and with data assimilation of surface pressure observations.
257 ~~Various~~ Several indices used to describe known modes of climate variability ~~are obtained from~~
258 ~~NOAA's Climate prediction Center (CPC) (<https://www.esrl.noaa.gov/psd/data/climateindices/list/>),~~
259 ~~which~~ include Arctic oscillation (AO), Northern Atlantic Oscillation (NAO), Atlantic Multidecadal
260 Oscillation (AMO) (Enfield et al., 2001) and PDO (Mantua et al., 1997) ~~indices.~~ are obtained from
261 NOAA's Climate prediction Center (CPC) (<https://www.esrl.noaa.gov/psd/data/climateindices/list/>).

262 2.2 Methods

263 From the perspective of nonlinear dynamic, a region's climate has its intrinsic modes of variability.

264 but the frequency of occurrence of these internal modes can be modulated by remote forces external to
265 the region (Palmer, 1999; Hoskins and Woollings, 2015; Shepherd, 2016). In this study we will first
266 obtain the main modes of variability of wintertime surface temperature in a region (40-90°N, 20-130°E)
267 by applying the SOM method (Kohonen, 2001) to daily surface temperature data for the 40 winters
268 (December, January, -February) in the 1979-2019 period from December 1979 through February 2019.
269 The use of daily data over four decades allows for capturing the variability across two time scales
270 (synoptic and decadal). ~~The 40-year, daily surface temperature over the study region (40-90°N,~~
271 ~~20-130°E) is decomposed using the SOM method.~~ SOM is a clustering method based on neural
272 network that can transform multi-dimensional data into a two-dimensional array without supervised
273 learning. The array includes a series of nodes arranged by a Sammon map (Sammon, 1969). Each node
274 in the array has a vector that can represent a spatial pattern of the input data. The distance of any two
275 nodes in the Sammon map represents the level of similarity between the spatial patterns of the two
276 nodes. Because SOM has fewer limitations than most other commonly used clustering methods, (e.g.,
277 orthogonality required by the empirical orthogonal function or EOF method), the SOM method can
278 describe better the main variability patterns of the input data (Reusch et al., 2005).

279 SOM method has been used in atmospheric research at mid and high latitudes of the northern
280 hemisphere (Skific et al., 2009; Johnson and Feldstein, 2010; Horton et al., 2015; Loikith and Broccoli,
281 2015; Vihma et al., 2019). For example, Johnson and Feldstein (2010) used SOM to identify~~ied the~~
282 spatial patterns of ~~the~~ daily wintertime North Pacific sea level pressure and related ~~ed~~ the variability of the
283 occurrences of those patterns to some large-scale circulation indices. Loikith and Broccoli (2015)
284 compared observed and model-simulated circulation patterns across the North American domain using
285 an approaching involving SOM. The SOM method was also used to detect circulation pattern trends in

286 a subset of North America during two [different](#) periods (Horton et al., 2015).
287 In this study, the SOM method is applied to [ERA-Interim](#) wintertime daily temperature anomalies [from](#)
288 [December 1979 through February 2019. The anomalies are calculated](#)~~obtained~~ by subtracting 40-year
289 averaged daily temperature from the original daily temperature at each grid point. Prior to SOM
290 analysis, it is necessary to determine how many SOM nodes are needed to best capture the variability
291 in the data. According to previous studies (Lee and Feldstein, 2013; Gibson et al., 2017; Schudeboom
292 et al., 2018), the rule for determining the number of SOM nodes is that the number should be
293 sufficiently large to capture the variability of the data analyzed, but not too large to introduce
294 unimportant details. Table 1 shows the averaged spatial correlation between all daily surface air
295 temperature [anomalies](#) and their matching nodes. ~~There is an increase in~~ [The spatial](#) correlation
296 coefficients [increase](#) from 0.26 for a 3×1 grid to 0.51 for a 4×4 grid, but the gain from a 3×3 grid to a
297 4×4 grid is relatively small. Hence, a 3×3 grid seems to meet the above-mentioned rule and will be
298 utilized in this study.

299 The contribution of each SOM node to the trend in wintertime surface temperature [anomalies](#) is
300 calculated by the product of each node pattern and its frequency trend normalized by the total number
301 [\(90\)](#) of wintertime days ~~(90,~~ Lee and Feldstein, 2013). The sum of the contributions from all nodes
302 denotes the SOM-explained trends. Residual trends are equal to the subtraction of SOM-explained
303 trends from the total trends. [The anomalous atmospheric circulation pattern corresponding to each of](#)
304 [the SOM pattern is obtained by composite analysis that computes a composite mean of an atmospheric](#)
305 [circulation field \(e.g., 500 hPa height\) over all occurrences of that SOM node. Regression analysis is](#)
306 [also performed where atmospheric circulation variables are regressed onto the time series of the](#)
307 [occurrence of a SOM node to further elucidate the relationship between the variability of atmospheric](#)

308 [circulations and surface temperatures](#). The statistical significance [of composite and regression analyses](#)
309 in this study is tested by using the Student's t test.

310 **3 Results**

311 3.1 Surface temperature variability

312 The majority of the 9 SOM nodes depict a dipole pattern characterized by opposite changes in
313 [surface temperatures](#) between the Arctic Ocean and the Eurasian continent, although the sign switch
314 does not always occur at the continent-ocean boundary (Figure 1). The [differences in the](#) position of the
315 boundary between the warm and cold anomalies [reflects](#) the transition between the cold Arctic-warm
316 Eurasia pattern (denoted, in descent order of the occurrence frequency, by nodes 3, 9, 6), to the warm
317 Arctic-cold Eurasia pattern (depicted, in descent order of the occurrence frequency, by nodes 1, 7, 4).

318 The spatial patterns represented by the first group of nodes (~~3, 9, 6~~) are almost mirror images of the
319 patterns denoted by the corresponding nodes in the second group (~~1, 7, 4~~). For example, the ~~first-second~~
320 node in group 1 (node 9, 15.4%) and [the first node](#) in group 2 (node 1, 17.1%) show a mirror image
321 pattern with cold (warm) anomalies in the Arctic Ocean extending into northern Eurasia and warm
322 (cold) anomalies in the rest of the Eurasia continent in the study domain. In both cases, the region of
323 maximum ~~anomalies-magnitude anomalies~~ is centered near Svalbard, Norway. The second ~~most~~
324 ~~frequent-patternpair~~, denoted by node 3 (17.2%) and 7 (13.7%) ~~in the two groups, respectively~~, has the
325 boundary of separation moved northward from northern Eurasia continent toward the shore of the
326 Arctic Ocean. While the maximum anomaly in the Arctic Ocean remains close to Svalbard, maximum
327 values over the continent are found in central Russia. Nodes 4-6 display a noticeable transition from
328 node 1 to node 7 and from node 3 to node 9, respectively. Although nodes 2 and 8 show an
329 approximate monopole spatial pattern, they also represent a transition between nodes 1 and 3, and

330 between nodes 7 and 9, respectively. Above SOM analysis ~~cannot~~does not consider the trend in surface
331 air temperature. The result is similar ~~while when removing~~ the trend is removed (~~Not-not~~ shown).

332 The temporal variability on this time scale is typically related to synoptic processes and hence the
333 questions are what synoptic patterns are responsible for the occurrence of the spatial patterns depicted
334 by each of the 9 SOM nodes and how these patterns are related to those of the Arctic sea ice anomalies?

335 These questions can be answered by using the composite method. Specifically, for each SOM node,
336 composite maps are made respectively for the anomalous 500-hPa geopotential height, mean sea level
337 pressure, 850-hPa wind, downward longwave radiation, surface turbulent heat flux, and sea ice
338 concentration over all the days when the spatial variability of the surface temperature anomalies is best
339 matched by the spatial pattern of that node.

340 3.2 Large-scale circulation patterns

341 For all SOM nodes, the spatial pattern of the composited 500 hPa-geopotential height anomalies
342 (Figure 2) is similar to that of mean sea level pressure anomalies (~~Not-not~~ shown), indicating an
343 approximately barotropic structure. For nodes 1, 4 and 7, the 500-hPa height anomalies show a dipole
344 structure of positive values over Siberia and negative values to its south over the Eurasian continent.

345 Anomalous southwesterly winds on the western side of the anticyclone over Siberia transport warm
346 and moist air from northern Europe and the North Atlantic Ocean into the Atlantic sector of the Arctic
347 Ocean (Figure 3), providing a plausible explanation of the warm surface temperature anomalies in the
348 region (Figure 1). On the eastern side of the anticyclone, anomalous northwesterly winds bring cold
349 and dry air from the Arctic Ocean into Eurasia continent, which is consistent with the negative surface
350 temperature anomalies there. The opposite occurs for nodes 3, 6 and 9. A similar explanation involving
351 anomalous pressure and wind fields can be applied to other nodes. The dipole structure that dominates

352 the anomalous 500-hPa height fields over the North Atlantic Ocean for most nodes resembles the
353 spatial pattern of the NAO (Figure 2). In addition, the patterns for ~~several~~ a few nodes, such as nodes 4
354 and 7, have some resemblance to the spatial pattern of the AO over larger geographical region. The
355 possible connection to NAO and AO is further investigated by averaging the daily index values of
356 NAO or AO over all occurrence days for each node. The results (Table 2) show that nodes 1, 2, 3 (5, 8,
357 9) correspond to a significant positive (negative) phase of the NAO index characterized by negative
358 (positive) height anomalies over Iceland and positive (negative) values over the central North Atlantic
359 Ocean. Association is also found between nodes 1, 2, 3, and 6 (5, 7, 8, and 9) and the positive (negative)
360 phases of the AO index.

361 3.3 Downward radiative fluxes

362 Besides the anomalous circulation patterns, anomalous surface radiative fluxes may also play a role in
363 shaping the spatial pattern of surface temperature variability. In fact, the spatial pattern of the mean
364 anomalous daily downward longwave radiation for an individual node (Figure 4) is in good agreement
365 with the spatial pattern of the surface temperature anomalies of that node. In other words, increased
366 downward longwave radiation is associated with positive surface temperature anomalies, and vice
367 versa. As expected from previous studies (e.g., Sedlar et al. 2011), there is a significant positive
368 correlation between downward longwave radiative fluxes and the anomalous total column water vapor
369 and mid-level cloud cover (not shown). The correlation to low- and high-level cloud cover is, however,
370 not significant (~~Not~~ not shown). Most of the water vapor in both the Arctic and Eurasia is derived from
371 the North Atlantic Ocean, but the water vapor is transported into the Arctic by southwesterly flows and
372 into Eurasia by northwesterly winds. The anomalous shortwave radiation corresponding to each node
373 (not shown) is an order of magnitude smaller than that of the longwave radiation anomalies and has a spatial

374 pattern opposite to that of the mid-level cloud cover and the longwave radiation anomalies.

375 3.4 Sea ice

376 The analyses presented above attempt to explain the spatial pattern of surface temperature
377 variability for each node from the perspective of anomalous heat advection and surface radiative fluxes.

378 As mentioned earlier, there has been a debate in the literature about the role played by the sea ice
379 anomalies in the Barents and Kara Seas in the development of the warm Arctic-cold Eurasia pattern.

380 Here, we examine the anomalous turbulent heat flux (Figure 5) and sea ice concentration (Figure 6) for
381 each node. Turbulent heat flux is considered positive when it is directed from the atmosphere
382 downward to the ocean or land surfaces. Thus, a positive anomaly indicates either an increase in the
383 atmosphere-to-surface heat transfer or a decrease in the heat transfer from the surface to the atmosphere.

384 The magnitude of anomalous turbulent heat flux is found to be comparable to that of anomalous
385 downward longwave radiation (Figure 4). For all nodes, the heat flux anomalies are larger over ocean

386 than over land [\(Figure 5\)](#). For node 1, positive turbulent heat flux anomalies occur mainly over the

387 Barents Sea, the western and central North Atlantic Ocean and the eastern North Pacific Ocean,
388 indicating an increase in heat transport from the air to the ocean due possibly to an increase in vertical

389 temperature gradient caused by warm air advection associated with anomalous circulation [\(Figures 2](#)
390 [and 3\)](#). The downward heat transfer results in sea ice melt in the Greenland Sea and the Barents Sea

391 (Figure 6). For node 4, the anomalous southerly winds over the Nordic Sea produce larger positive

392 turbulent heat flux anomalies [\(Figure 5\)](#). For node 7, the anticyclone is located more northwards, which

393 generates opposite anomalous winds between the Nordic and northern Barents Seas and the southern

394 Barents Sea and thus opposite turbulent heat flux anomalies that are consistent with the opposite sea ice

395 concentration anomalies in the two regions [\(Figure 5\)](#). For nodes 3, 6, and 9, the anomalous cold air

396 from the central Arctic Ocean flows into warm water in the Nordic and Barents Seas, producing
397 negative turbulent heat flux anomalies and positive sea ice concentration anomalies ([Figures 5 and 6](#)).
398 Sorokina et al. (2016) noted that turbulent heat flux usually peaks 2 days before changes in surface
399 temperature pattern occur. The pattern of the composited anomalous [500-hPa geopotential height](#),
400 turbulent heat flux [and sea ice concentration](#) 2 days prior to the day when the nodes occur (not shown)
401 is similar to the current-day pattern in [Figures 2, 65, and 6](#). Our results support the conclusion of
402 Sorokina et al. (2016) and Blackport et al. (2019) that the anomalous atmospheric circulations lead to
403 the anomalous sea ice concentration in the Barents Sea.

404 ~~3.5 Contributions of SOM nodes to the~~ Trends in wintertime surface temperature

405 The results above suggest that both the surface temperature anomaly patterns over the Arctic Ocean
406 and Eurasian continent and the sea ice concentration anomalies in the Nordic and Barents Seas can be
407 explained largely by changes in atmospheric circulations and the associated vertical and horizontal heat
408 and moisture transfer by mean and turbulent flows. Next, we assess the [trends of wintertime surface](#)
409 [temperature and the](#) contributions of these [SOM](#) nodes to the ~~trends in wintertime surface temperature~~.

410 We first examine the time series of the accumulated number of days for each node in each winter
411 for the 1979-2019 period (Figure 7). The time series for nodes 1, 4, 6, and 9 exhibit variability on
412 interannual as well as decadal time scales. The occurrence frequency is noticeably larger after 2003
413 than prior to 2003 for nodes 1 and 4, and vice versa for nodes 6 and 9, and the difference between the
414 two periods is significant at 95% confidence level. Given the spatial patterns of these four nodes
415 (Figure 1), this indicates that the warm Arctic-cold Eurasia pattern occurred more frequently after 2003.
416 A linear trend analysis of the time series for each node (Table [23](#)) reveals significant positive trends in
417 occurrence frequency for nodes 1 and 4 and significant negative trends for nodes 6 and 9, which agree

418 | with the result from a previous study (Clark and Lee, 2019; [Overland et al., 2015](#)) that suggested an
419 | increasing trend of the warm Arctic and cold Eurasia pattern.

420 | These trends in the occurrence frequency of the SOM nodes contribute to the trends in the total
421 | wintertime (DJF) surface temperature anomalies (Figure 8, top panel) that have significant positive
422 | trends over the Arctic Ocean and in regions of Northern and ~~Southern~~-Eastern Europe and negative,
423 | [mostly insignificant](#) trends in Central Siberia. The contribution, however, varies from node to node
424 | (Figure 9). Node 1 has the largest domain-averaged contribution of 18.7%, followed by its mirror node
425 | (node 9) at 10.1%. Nodes 4 and 6 account for 2.8% and 4.3% of the total trend, respectively. None of
426 | the remaining nodes explain more than 2%. All nodes together explain 39.5% of the total trend in
427 | wintertime surface air temperature. The spatial pattern of the SOM-explained trends (Figure 8, middle
428 | panel) is similar to the warm Arctic–cold continent pattern, whereas the residual trend resembles more
429 | the total trend (Figure 8 bottom panel).

430 | 3.6 Mechanisms

431 | The results presented above indicate that the SOM patterns explain nearly 40% of the trend in
432 | wintertime surface air temperature anomalies and majority of the contributions (35 out of 40%) come
433 | from the two pairs of the nodes (nodes 1, 9, and 4, 6). –The analyses hereafter will focus on these four
434 | nodes. Below we assess the atmospheric and oceanic conditions associated with the occurrences of the
435 | four nodes via regression analysis. Specifically, the anomalous seasonal SST and atmospheric
436 | circulation variables are regressed onto the normalized time series of the number of days when each of
437 | the four nodes occurs (Figures 10, 11, and 12).

438 | For node 1, the SST regression pattern in the Pacific Ocean shows significant positive anomalies
439 | over the tropical western Pacific Ocean and central North Pacific Ocean ([Figure 10](#)). The positive SST

440 anomalies also occur over most of the North Atlantic. Negative SST anomalies occur over the central
441 tropical Pacific Ocean, though they are not significant at 95% confidence level. The SST regression
442 pattern is reversed for node 9. The direction of wave activity flux indicates the direction of group speed
443 of stationary planetary wave. Here we calculate the wave activity flux defined by Takaya and
444 Nakamura (2001), which considers the influence of mid-latitude zonal wind (Figure 12). For node 1,
445 ~~The~~ the corresponding anomalous 500-hPa height regression (Figure 11) shows two Rossby wavetrains:
446 one is excited over the central Pacific Ocean and propagates northeastwards into North America and
447 North Atlantic Ocean, and the other, which displays ~~a~~ the stronger signal, originates from central North
448 Atlantic and propagates northeastwards to the Arctic Ocean and southeastwards to the Eurasian
449 continent ~~and the western Pacific Ocean (Figure 11 and 12). The large SST anomalies over the Nordic~~
450 ~~Ocean augment the wave signal through local air sea interaction. The wave activity flux and~~
451 ~~streamfunction exhibit well the horizontal propagating direction of the planetary wave.~~ For node 9, the
452 corresponding anomalous 500-hPa height and streamfunction show an opposite pattern, but the wave
453 activity flux is similar to that of node 1.

454 For node 4, the SST anomalies over the tropical Pacific Ocean appear to be in a La Niña state,
455 which shows stronger negative SST anomalies over the eastern tropical Pacific Ocean than those for
456 node 1 (Figure 10). The positive SST anomalies over the North Pacific shift more northwards relative
457 to that of node 1. The positive SST anomalies over the North Atlantic are weaker than those for node 1.
458 The corresponding wavetrain over the Pacific Ocean is stronger than that over the Atlantic Ocean
459 (Figure 11), which ~~is~~ seen also be observed in the pattern of wave activity and streamfunction (Figure
460 12). The corresponding pattern for node 6 is nearly reversed, but there are some noticeable differences
461 in the amplitude of the wavetrain and SST anomalies. For example, the magnitude of the anomalous

462 SST and the 500-hPa height over the central North Pacific is larger for node 6 than that for node 4.

463 Besides the above-mentioned variables, similar regression analysis is also performed for the
464 anomalous 850-hPa wind field and anomalous downward longwave radiation (~~Not-not~~ shown). Their
465 regression patterns, which are similar to those in Figures 3 and 4, explain well the decadal variability of
466 the number of days for nodes 1, 4, 6, and 9. Together, these results [in Figures 10-12](#) indicate that the
467 decadal variability of the occurrence frequency of the four nodes in recent decades is related to two
468 wavetrains induced by SST anomalies over the central North Pacific Ocean and the North Atlantic
469 Ocean ([Figures 10 and 11](#)). The aforementioned SST regression patterns over the Atlantic and Pacific
470 Oceans also show features of the AMO and PDO (Figure 10). Since both the AMO and PDO exhibited
471 a phase change in the late 1990s (Yu et al., 2017), the question is whether a similar change in the SOM
472 frequency also appear in the late 1990s. A comparison of the averaged frequency before and after 1998
473 shows a significant drop in frequency for nodes 6 and 9 and an increase in frequency for node 1 (~~not~~
474 [shown](#)). This result suggests that the change in the AMO and PDO indices may contribute to the change
475 in the frequencies of the warm Arctic-cold Eurasia continent pattern.

476 3.7 Interdecadal variability

477 The four-decade-long ERA-Interim reanalysis is not adequate for examining interdecadal to
478 multi-decadal variations represented by the PDO and AMO indices. Further analysis is performed using
479 the 20CR daily reanalysis data for the 1854-2014 period. Before applying the SOM technique to the
480 20CR data, we first remove the trend to eliminate the influence from the global warming. No low-pass
481 filter is applied before SOM analysis in order to test the stability of the SOM results for the different
482 periods. The spatial SOM patterns from the de-trended century-long 20CR data (Figure 13) are similar
483 to those for the 1979-2019 period (Figure 1). Nodes 1, 4, and 7 correspond to the positive phase of the

484 warm Arctic-cold Eurasia pattern and the negative phase can be observed in nodes 3, 6, and 9. The
485 magnitude [in Figure 13](#) is smaller compared to the recent four decades [in Figure 1](#). The occurrence
486 frequencies of ~~all~~ the [four nodes, 1, 4, 6, and 9](#) (Figure 14), are close to those for the recent four
487 decades ([Figure 7](#)). It indicates that the SOM method can obtain stably the main modes of wintertime
488 surface air temperature variability. For the recent four decades, the time series of the number of days
489 also displays a noticeable increasing (decreasing) trend for nodes 1 and 4 (6 and 9), suggesting that the
490 trend in the recent four decades is a reflection of an interdecadal variability of wintertime surface air
491 temperature.

492 Next, we apply a 40-year low-pass filter to the time series of the occurrence frequencies for nodes
493 1, 4, 6 and 9 and the AMO and PDO indices and calculate correlations. There is a significant
494 correlation between the time series and the AMO index, with correlation coefficients of 0.36 for node 1,
495 0.27 for node 4, -0.37 for node 6, and -0.20 for node 9, all of which are at the 95% confidence level. No
496 significant correlations, however, are found between the filtered time series and the PDO index. If we
497 define ~~a~~ SST index to represent the variability of SST anomalies over the central North Pacific Ocean
498 (20°N-40°N, 150°E-150°W), the 40-year low-pass filtered central North Pacific Ocean SST index is
499 now significantly correlated with the filtered time series of occurrence frequencies for nodes 1 and 9
500 (0.55 for node 1 and -0.46 for node 9). The [correlation](#) results are consistent with the SST regression
501 map for the recent decades (Figure 10).

502 To confirm the effect of SST anomalies on the warm Arctic -cold Eurasia pattern, we also perform
503 EOF analysis of wintertime detrended seasonal surface air temperature anomalies for the 1854-2014
504 period (Figure 15). The spatial patterns of the first and second EOF modes show the negative phase of
505 the warm Arctic-cold Eurasia pattern and the 40-year low-pass filtered time series is inversely

506 correlated with the 40-year low-pass filtered wintertime AMO index (-0.46, $p < 0.05$ for mode 1 and
507 -0.44, $p < 0.05$ for mode 2). The 40-year low-pass filtered time series of the two EOF modes have a
508 significant negative correlation with the 40-year low-pass filtered central North Pacific Ocean SST
509 index, with correlation coefficients of -0.19 and -0.26 ($p < 0.05$). Only PC1 has a significant correlation
510 with the PDO index (0.38, $p < 0.05$). Thus, the increase in the occurrence of the warm Arctic-cold
511 Eurasia pattern in the recent decades is a part of the interdecadal variability of the pattern, which is
512 influenced by the AMO index, [the PDO index](#), and the central North Pacific SST.

513 **4 Conclusions and Discussions**

514 In this study, we examine the variability of wintertime surface air temperature in the Arctic and the
515 Eurasian continent (20°E-130°E) by applying the SOM method to daily temperature from the gridded
516 ERA-Interim dataset for the period 1979-2019 and from the 20CR reanalysis for the period 1854-2014
517 and the EOF method to seasonal temperature from the 20CR reanalysis for the period 1854-2014. The
518 spatial pattern in the surface temperature variations in the study region, as revealed by the nine SOM
519 nodes, is dominated by concurrent warming in the Arctic and cooling in Eurasia, and vice versa. The
520 nine SOM patterns explain nearly 40% of the trends in wintertime surface temperature and 88% of that
521 are accounted for by only four nodes. Two of the four nodes (nodes 1 and 4) represent the warm
522 Arctic-cold Eurasian pattern and the other two (nodes 6 and 9) depict the opposite cold Arctic-warm
523 Eurasia pattern. There is a clear shift in the frequency of the occurrence of these patterns near the
524 beginning of this century, with the warm Arctic – cold Eurasia pattern dominating since 2003, while the
525 opposite pattern prevailing from the 1980s through the 1990s. The warm Arctic-cold Eurasia pattern is
526 accompanied by an anomalous high pressure and anticyclonic circulation over the Eurasian continent.
527 The anomalous winds and the associated temperature and moisture advection interact with local

528 | longwave radiative forcing and turbulent [fluxes](#) to produce positive (negative) temperature anomalies
529 | in the Arctic (Eurasian continent). The circulation is reversed for the cold Arctic-warm Eurasia pattern.
530 | The warm, moist air mass advected to the Arctic by the anomalous atmospheric circulations and the
531 | increased downward turbulent heat flux also explain sea ice melt in the Barents and Kara Seas. In other
532 | words, the sea ice loss in the Barents and Kara Seas and the cooling of the Eurasian continent can both
533 | be traced to anomalous atmospheric circulations.

534 | Increasing occurrences of the warm Arctic-cold Eurasian continent pattern appear to relate to
535 | rising SST over the central North Pacific and North Atlantic Oceans (positive AMO phase). The SST
536 | anomalies trigger two Rossby wavetrains spanning from the North Pacific Ocean, North America, and
537 | the North Atlantic Ocean to the Eurasian continent. The two wavetrains are strengthened through local
538 | sea-atmosphere-ice interactions in mid-high latitudes, which influence the change in the occurrence
539 | frequency of the warm Arctic-cold Eurasian continent pattern. Our results agree with those of previous
540 | studies (Lee et al., 2011; Sato et al., 2014; Clark and Lee, 2019). But previous studies only focus on the
541 | [effects](#) of SST anomalies over either North Pacific or North Atlantic Oceans. We also note that the two
542 | wavetrains excited by SST anomalies over different oceans differ in amplitudes, leading to somewhat
543 | different warm Arctic-cold Eurasia patterns.

544 | Using century-long data, we show that the warm Arctic-cold Eurasia pattern is an intrinsic climate
545 | mode, which has been stable since 1854. The recent increasing trend in its occurrence is a reflection of
546 | an interdecadal variability of the pattern resulting from the interdecadal variability of SST anomalies
547 | over the central Pacific Ocean and over the Atlantic Ocean represented by the AMO index. Sung et al.
548 | (2018) investigated interdecadal variability of the warm Arctic and cold Eurasia pattern and considered
549 | the variability of the SST over the North Atlantic as its origin. Our results suggest that the variability of

550 the SST over the North Pacific also plays an important role. However, internal atmospheric variability
551 remains another potential source. The Rossby wavetrains also lead to deepening of a trough in East
552 Asia and generate an anomalous low [pressure](#) and cold temperature in northern China ([Figure 10](#)),
553 which further suggests that ~~the relationship between~~ a warmer Arctic, especially warmer Barents and
554 Kara Seas ~~, and is not the driver for~~ the [increasing](#) occurrence of cold spells in East Asia, [as](#)
555 [suggested in](#) ~~may not be as strong as~~ [previously thought studies](#) (Kim et al., 2014; Mori et al., 2014;
556 Kug et al., 2015; Overland et al., 2015).

557 [Our results suggest that the increasing trend in warm Arctic-cold Eurasia pattern may be related to](#)
558 [the anomalous SST over the central North Pacific and the North Atlantic Oceans. But we cannot rule](#)
559 [out the influence of the Arctic sea ice loss on the trend. Because the](#) ~~The Arctic sea ice loss results from~~
560 [two main drivers: external and internal forcings. The former refers to the both Arctic warming due to](#)
561 [anthropogenic increasing of greenhouse gas concentrations and natural variability of ; the latter comes](#)
562 [from the climate system internal variability, such as anomalous SST anomalies. This study considers](#)
563 [natural variability or only the internal driver of climate system. The Arctic warming caused external](#)
564 [forcing related to increasing greenhouse gas emissions can produce an anomalous anticyclone over the](#)
565 [Barents and Kara Seas, leading to the warm Arctic-cold continents pattern.](#)

566 [Although the ERA-Interim reanalysis is overall superior in describing](#) ~~has the best performance in~~
567 [overall depiction of the Arctic atmospheric environment to other similar global reanalysis products, it](#)
568 [contains](#) ~~includes~~ [warm and moist biases in the surface layer \(Jakobson et al., 2012; Chaudhuri et al.,](#)
569 [2014; Simmons and Poli, 2015; Wang et al., 2019\). However, we believe these biases, as well as the](#)
570 [relatively coarse resolution, should have minimum impact in the results from the current analyses.](#)
571 [Further, although the current analyses were performed on a predetermined SOM grid with 3x3 nodes,](#)

572 [an increase in the number of SOM nodes didn't change the conclusions.](#)

573 Our results help broaden the current understanding of the formation mechanisms for the warm
574 Arctic-cold Eurasia pattern. The SST anomalies over Northern Hemisphere oceans may offer a
575 potential for predicting its occurrence. [The statistical relationship between SST anomalies and the](#)
576 [occurrences of the warm Arctic-cold continents pattern may help improve the predictability of](#)
577 [wintertime surface air temperature over Eurasian continent on interdecadal time scales.](#)

578 **Data Availability**

579 All data used in the current analyses are publicly available. The monthly sea ice concentration data are
580 available from the National Snow and Ice Data Center (NSIDC) (<http://nsidc.org/data/NSIDC-0051>), the
581 ERA-Interim reanalysis data are available from the European Center for Mid-Range Weather
582 Forecasting (<https://www.ecmwf.int/en/forecasts/datasets/reanalysis-datasets/era-interim>) and the sea
583 surface temperature data are available from the Hadley Centre for Climate Prediction and Research
584 (<ftp://ftp.cdc.noaa.gov/Datasets/noaa.oisst.v2.highres/>). The long-term SST data are derived from
585 from the Twentieth Century Reanalysis project, version 2c (20CR)
586 (<https://climatedataguide.ucar.edu/climate-data/noaa-20th-century-reanalysis-version-2-and-2c>).

587 **Competing interests**

588 The authors declare that they have no conflict of interest.

589 **Author Contributions**

590 L. Yu designed the study, with input from S. Zhong, and carried out the analyses. L. Yu and S. Zhong
591 prepared the manuscript. C. Sui plotted a part of Figures. [-B. Sun revised the manuscript.](#)

592 **Acknowledgements** We thank the European Centre for Medium-Range Weather Forecasts (ECMWF)
593 for the ERA-Interim data. This study is financially supported by the National Key R&D Program of
594 China (2019YFC1509102; 2017YFE0111700) and the National Natural Science Foundation of China
595 (41922044).

596

597

598

599

600

601

602

603

604

605

606

607 **References**

608 Barnes, E. A. and Screen, J. A.: The impact of Arctic warming on the midlatitude jet-stream: Can it?

609 Has it? Will it?, WIREs Clim. Change, 6, 277-286, doi:10.1002/wcc.337, 2015.

610 Blackport, R., Screen J. A., Wiel K. van der, and Bintanja, R.: Minimal influence of reduced Arctic sea

611 ice on coincident cold winters in mid-latitudes, Nature Climate Change, 9,

612 doi:10.1038/s41558-019-0551-4, 2019, 2019.

613 [Chaudhuri, A. H., Ponte, R. M., and Nguyen, A. T.: A Comparison of atmospheric reanalysis products](#)

614 [for the Arctic Ocean and implications for uncertainties in air-sea fluxes, J. Climate, 27,](#)

615 [5411-5421, doi:10.1175/JCLI-D-13-00424.1, 2014.](#)

616 [Chen, L., Francis J. and Hanna E.: The “Warm-Arctic/Cold continents” pattern during 1901-2010.](#)

617 [Int. J. Climatol., 38, 5245-5254, ~~https://doi.org/doi:10.1002/joc.5725~~, 2018.](#)

618 Clark, J. P. and Lee, S.: The role of the tropically excited Arctic Warming Mechanism on the warm

619 Arctic cold continent surface air temperature trend pattern, *Geophys. Res. Lett.*, 46, 8490-8499,
620 doi:10.1029/2019GL082714, 2019

621 Cohen, J., Screen, J. A., Furtado, J. C., Barlow, M., Whittleston, D., Coumou, D., Francis, J., Dethloff,
622 K., Entekhabi, D., Overland, J., and Jones, J.: Recent Arctic amplification and extreme
623 mid-latitude weather, *Nat. Geosci.*, 7, 627-637, doi:10.1038/ngeo2234, 2014.

624 Cohen, J., Pfeiffer, K., and Francis, J. A.: Warm Arctic episodes linked with increased frequency of
625 extreme winter weather in the United States, *Nat. Commun.*, 9, 869,
626 doi:10.1038/s41467-018-02992-9, 2018.

627 Compo, G. P., Whitaker, J. S., Sardeshmukh, P. D., Matsui, N., Allan, R., Yin, X., Jr, G. B. E., Vose, R.
628 S., Rutledge, G. K., Bessemoulin, P., Brönnimann, S., Brunet, M., Crouthamel, R. I., Grant, A.
629 N., Groisman, P. Y., Jones, P. D., Kruk, M. C., Kruger, A. C., Marshall, G. J., Maugeri, M., Mok,
630 H. Y., Nordli, Ø., Ross, T. F., Trigo, R. M., Wang, X., Woodruff, S. D., and Worley S. J.: The
631 Twentieth Century Reanalysis Project, *Quart. J. Roy. Meteor. Soc.*, 137, 1-28,
632 doi:10.1002/qj.776, 2011.

633 Dee, D. P., Uppala, S. M., Simmons, A. J., Berrisford, P., Poli, P., Kobayashi, S., Andrac, U.,
634 Balmaseda, M. A., Balsamo, G., Bauer, P., Bechtold, P., Beljaars, A. C. M., van de Berg, L.,
635 Bidlot, J., Bormann, N., Delsol, C., Dragani, R., Fuentes, M., Geer, A. J., Haimberger, L., Healy,
636 S. B., Hersbach, H., Hõm, E. V., Isaksen, L., Kålberg, P., Köhler, Matricardi, M., McNally, A.
637 P., Monge-Sanz, B. M., Morcrette, J.-J., Park, B.-K., Peubey, C., de Rosnay, P., Tavolato, C.,
638 Thépaut, J.-N., and Vitart, F.: The ERA-Interim reanalysis: configuration and performance of the
639 data assimilation system. *Q. J. R. Meteorol. Soc.*, 137, 553-597, doi:10.1002/qj.828, 2011.

640 Enfield, D. B., Mestas-Nunez, A. M., and Trimble, P. J.: The Atlantic multidecadal oscillation and it's

641 relation to rainfall and river flows in the continental U.S., *Geophys. Res. Lett.*, 28, 2077-2080,
642 2001.

643 Fyfe, J. C.: Midlatitudes unaffected by sea ice loss. *Nature Climate Change*, 9,
644 doi:10.1038/s41558-019-0560-3, 2019 .

645 Gibson, P. B., Perkins-Kirkpatrick, S. E., Uotila, P., Pepler, A. S., and Alexander, L. V.: On the use of
646 self-organizing maps for studying climate extremes, *J. Geophys. Res. Atmos.*, 122, 3891–3903,
647 [doi:10.1002/2016JD026256](https://doi.org/10.1002/2016JD026256), 2017.

648 Hoskins, B. and Woollings, T.: Persistent extratropical regimes and climate extremes. *Curr. Clim. Change*
649 *Rep.*, 1, 115-124, doi:10.1007/s40641-015-0020-8, 2015

650 Horton, D. E., Johnson, N. C., Singh, D., Swain, D. L., Rajaratnam, B., and Diffenbaugh, N. S.:
651 Contribution of changes in atmospheric circulation patterns to extreme trends, *Nature*,
652 522,465-469, doi:10.1038/nature14550, 2015.

653 Inoue, J., Hori, M. E., and Takaya, K.: The role of Barents Sea ice in the wintertime cyclone track and
654 emergence of a warm-Arctic-Siberian anomaly, *J. Clim.*, 25, 2561-2568,
655 doi:10.1175/JCLI-D-11-00449.1, 2012.

656 Jakobson, E., Vihma, T., Palo, T., Jakobson, L., Keernik, H., and Jaagus, J.: Validation of atmospheric
657 reanalyses over the central Arctic Ocean, *Geophys. Res. Lett.*, 39, L10802,
658 doi:10.1029/2012GL051591, 2012.

659 Johnson, N. C. and Feldstein, S. B.: The continuum of North Pacific sea level pressure patterns:
660 Intraseasonal, interannual, and interdecadal variability, *J. Clim.*, 23,
661 851-867, doi:10.1175/2009JCLI3099.1, 2010.

662 [Jakobson, E., Vihma, T., Palo, T., Jakobson, L., Keernik, H., Jaagus, J.: Validation of atmospheric](#)

663 | [reanalyses over the central Arctic Ocean, *Geophys. Res. Lett.*, 39, 2012.](#)

664 Kalnay, E., Kanamitsu, M., Kistler, R., Collins, W. G., Deaven, D., Gandin, L., Iredell, M., Saha, S.,
665 White, G., Woollen J.: The NCEP/NCAR 40-year reanalysis project, *Bull. Amer. Meteor. Soc.*,
666 77, 437-471, doi:10.1175/1520-0477(1996)077<0437:TNYRP>2.0.CO;2, 1996.

667 Kim, B.-M., Son, S.-W., Min, S.-K., Jeong, J.-H., Kim, S.-J., Zhang, X., Shim, T., and Yoon, J.-H.:
668 Weakening of the stratospheric polar vortex by Arctic sea-ice loss, *Nature Commun.*, 5, 4646,
669 doi:10.1038/ncomms5646, 2014.

670 Kohonen, T.: *Self-Organizing Maps*. 3rd ed. Springer, 501 pp, 2001.

671 Kug, J.-S., Jeong, J.-H., Jang, Y.-S., Kim, B.-M., Folland, C. K., Min, S.-K., and Son, S.-W.: Two
672 distinct influences of Arctic warming on cold winters over North America and East Asia, *Nat.*
673 *Geosci.*, 8, 759-762, doi:10.1038/ngeo2517, 2015.

674 Lee, S., Gong, T., Johnson, N., Feldstein, S. B., and Pollard, D.: On the possible link between tropical
675 convection and the Northern Hemisphere Arctic surface air temperature change between 1958
676 and 2001, *J. Clim.*, 24, 4350-4367, doi:10.1175/2011JCLI4003.1, 2011.

677 Lee, S. and Feldstein, S. B.: Detecting ozone- and greenhouse gas-driven wind trends with
678 | observational data, *Science*, 339, 563-567, [doi:10.1126/science.1225154](#), 2013.

679 Loikith, P. C. and Broccoli, A. J.: Comparison between observed and model-simulated atmospheric
680 circulation patterns associated with extreme temperature days over North America using CMIP5
681 historical simulations, *J. Clim.*, 28, 2063-2079, doi:10.1175/JCLI-D-13-00544.1, 2015.

682 Luo, D., Xiao, Y., Yao, Y., Dai, A., Simmonds, I., and Franzke, C. L. E.: Impact of Ural blocking on
683 winter warm Arctic-cold Eurasian anomalies. Part I: Blocking-induced amplification, *J. Clim.*,
684 29, 3925-3947, doi:10.1175/JCLI-D-15-0611.1, 2016.

685 Mantua, N. J., Hare, S. R., Zhang, Y., Wallace, J. M., and Francis, R. C.: A Pacific interdecadal climate
686 oscillation with impacts on salmon production, *Bull. Amer. Meteor. Soc.*, 78, 1069–1079, 1997.

687 Matsumura, S. and Kosaka, Y.: Arctic-Eurasian climate linkage induced by tropical ocean variability,
688 *Nature Communications*, 10, 3441, doi:10.1038/s41467-019-11359-7, 2019.

689 Mori, M., Watanabe, M., Shiogama, H., Inoue, J., and Kimoto, M.: Robust Arctic sea-ice influence on
690 the frequent Eurasian cold winters in past decades, *Nat. Geosci.*, 7, 869-873,
691 doi:10.1038/ngeo2277, 2014.

692 Mori, M., Kosaka, Y., Watanabe, M., Nakamura, H., and Kimoto, M.: A reconciled estimate of the
693 influence of Arctic sea-ice loss on recent Eurasian cooling, *Nat. Clim. Change*, 9, 123-129,
694 doi:10.1038/s41558-018-0379-3, 2019.

695 McCusker, K. E., Fyfe, J. C., and Sigmond, M.: Twenty-five winters of unexcepted Eurasian cooling
696 unlikely due to Arctic sea-ice loss, *Nat. Geosci.*, 9, 838-842, doi:10.1038/ngeo2820, 2016.

697 Overland, J. E., Wood, K. R., and Wang, M.: Warm Arctic-cold continents: climate impacts of the
698 newly open Arctic sea, *Polar Res.*, 30, 15787, doi:10.3402/polar.v30i0.15787, 2011.

699 Overland, J. E., Francis, J., Hall, R., Hanna, E., Kim, S.-J., and Vihma, T.: The melting Arctic and
700 Midlatitude weather patterns: Are they connected?, *J. Clim.*, 28, 7917-7932,
701 doi:10.1175/JCLI-D-14-00822.1, 2015.

702 Palmer, T. N.: A nonlinear dynamical perspective on climate prediction, *J. Clim.*, 12, 575-591, 1999.
703 doi:10.1175/1520-0442(1999)012<0575:ANDPOC>2.0.CO;2

704 Peings, Y.: Ural blocking as a driver of early-winter stratospheric warmings, *Geophys. Res. Lett.*, 46,
705 5460-5468, doi:10.1029/2019GL082097, 2019.

706 Reusch, D. B., Alley, R. B., and Hewitson, B. C.: Relative performance of self-organizing maps and

707 principal component analysis in pattern extraction from synthetic climatological data, *Polar*
708 *Geogr.*, 29, 188–212, doi:10.1080/789610199, 2005.

709 Reynolds, R. W., Smith, T. M., Liu, C., Chelton, D. B., Casey, K. S., Schlax, M. G.: Daily
710 High-Resolution-Blended Analyses for Sea Surface Temperature, *J. Climate*, 20, 5473-5496,
711 doi:10.1175/2007JCLI1824.1, 2007.

712 Sammon, J. W.: A non-linear mapping for data structure analysis. *IEEE Trans. Computers*, C-18,
713 401–409 , 1969.

714 Sato, K., Inoue, J., and Watanabe, M.: Influence of the Gulf Stream on the Barents Sea ice retreat and
715 Eurasian coldness during early winter, *Environ. Res. Lett.*, 9, 084009,
716 doi:10.1088/1748-9326/9/8/084009, 2014.

717 Schudeboom, A., McDonald, A. J., Morgenstern, O., Harvey, M., and Parsons, S.: Regional
718 regime-based evaluation of present-day GCM cloud simulations using self-organizing maps, *J.*
719 *Geophys. Res. Atmos.*, 123, 4259–4272, doi:10.1002/2017JD028196, 2018.

720 Screen, J. A. and Simmonds, I.: The central role of diminishing sea ice in recent Arctic temperature
721 amplification, *Nature*, 464, 1334-1337, doi:10.1038/nature09051, 2010.

722 Screen, J. S. and Simmonds, I.: Erroneous Arctic temperature trends in the ERA-40 reanalysis: A closer
723 look, *J. Clim.*, 24, 2620–2627, doi:10.1175/2010JCLI4054.1, 2011.

724 Sedlar, J., Tjernström, M., Mauritsen, T., Shupe, M. D., Brooks, I. M., Persson, O., Birch, C. E., Leck,
725 C., Sirevaag, A., and Nicolaus, M. : A transitioning Arctic surface energy budget: The impacts of
726 solar zenith angle, surface albedo and cloud radiative forcing, *Clim. Dyn.*, 37, 1643–1660,
727 [doi:10.1007/s00382-010-0937-5](https://doi.org/10.1007/s00382-010-0937-5), 2011.

728 Shepherd, T. G.: Effects of a warming Arctic, *Science*, 353, 989-990, doi:10.1126/science.aag2349,

729 2016.

730 [Simmons, A., and Poli, P.: Arctic warming in ERA-Interim and other analyses, Q. J. R. Meteorol. Soc.,](#)
731 [141, 1147-1162, doi:10.1002/qj.2422, 2015.](#)

732 Skific, N., Francis, J. A., and Cassano, J. J.: Attribution of projected changes in atmospheric moisture
733 transport in the Arctic: A self-organizing map perspective, J. Clim., 22, 4135-4153,
734 doi:10.1175/2009JCLI2645.1, 2009.

735 Sorokina, S. A., Li, C., Wettstein, J. J., and Kvamstø N. G.: Observed atmospheric coupling between
736 Barents sea ice and the warm-Arctic cold-Siberian anomaly pattern, J. Clim., 29, 495-511,
737 doi:10.1175/JCLI-D-15-0046.1, 2016.

738 Stroeve, J. C., , Holland, M. M., Meier, W., Scambos, T., and Serreze, M.: Arctic sea ice decline: faster
739 than forecast, Geophys. Res. Lett., 34, L09051, doi:10.1029/2007gl029703, 2007.

740 Stroeve, J. C.: Trends in Arctic sea ice extent from CMIP5, CMIP3 and observations, Geophys. Res.
741 lett., 39, L16502, doi:10.1029/2012GL052676 , 2012.

742 Sun, L., Perlwitz, J., and Hoerling, M.: What caused the recent “warm Arctic-Cold Continents” trend
743 pattern in winter temperature?, Geophys. Res. Lett., 43, 5345-5352,
744 doi:10.1002/2016GL069024, 2016.

745 Sung, M.-K., Kim, S.-H., Kim, B.-M., and Choi, Y.-S.: Interdecadal variability of the warm Arctic and
746 cold Eurasia pattern and its North Atlantic origin, Journal of Climate, 31, 5793-5810,
747 doi:10.1175/JCLI-D-17-0562.1, 2018.

748 Tang, Q., Zhang, X., Yang, X., and Francis J. A.: Cold winter extremes in northern conditions linked to
749 Arctic sea ice loss, Environ. Res. Lett., 8, 014036, doi:10.1088/1748-9326/8/1/014036 ,2013.

750 Takaya K, and Nakamura, H.: A formulation of a phase-independent wave-activity flux for stationary

751 and migratory quasigeostrophic eddies on a zonally varying basic flow, *J. Atmos. Sci.*, 58,
752 608-627, 2001.

753 Uppala, S., KÅllberg, P. W., Simmons, A. J., Andrae, U., Da Costa Bechtold, V., Florino, M., Gibson, J.
754 K., Haseler, J., Hernandez, A., Kelly, G. A., Li, X., Onogi, K., Saarinen, S., Sokka, N., Allan, R.
755 P., Andersson, E., Arpe, K., Balmaseda, M. A., Beljaars, A. C. M., Van De Berg, L., Bidlot, J.,
756 Bormann, N., Caires, S., Chevallier, F., Dethof, A., Dragosavac, M., Fisher, M., Fuentes, M.,
757 Hagemann, S., Hm, E., Hoskins, B. J., Isaksen, L., Janssen, P. A. E. M., Jenne, R., McNally, A.
758 P., Mahfouf, J.-F., Morcrette, J.-J., Rayner, N. A., Saunders, R. W., Simon, P., Sterl, A.,
759 Trenberth, K. E., Untch, A., Vasiljevic, D., Viterbo, P., and Woollen, J.: The ERA-40 re-analysis,
760 *Quarterly Journal of the Royal Meteorological Society*, 131, 2961–3012, doi:10.1256/qj.04.176,
761 2005.

762 Walsh, J. E.: Intensified warming of the Arctic: Causes and impacts on middle Latitudes, *Glob. Planet.*
763 *Change*, 117, 52-63, doi:10.1016/j.gloplacha.2014.03.003 , 2014.

764 Vihma, T.: Effects of Arctic sea ice decline on weather and climate: A review, *Surv. Geophys.*, 35,
765 1175-1214, doi:10.1007/s10712-014-9284-0 , 2014.

766 Vihma, T., Graverson, R., Chen, L., Handorf, D., Skific, N., Francis, J. A., Tyrrell, N., Hall, R., Hanna,
767 E., Uotila, P., Dethloff, K., Karpechko, A. Y., Bj rnsson, H., and Overland, J. E.: Effects of the
768 tropospheric large-scale circulation on European winter temperatures during the period of amplified
769 Arctic warming, *Int. J. Climatol.*, doi:10.1002/joc.6225, 2019.

770 [Wang, C., Graham, R. M., Wang, K., Gerland, S., Granskog, M. A.: Comparison of ERA5 and](#)
771 [ERA-Interim near-surface air temperature, snowfall and precipitation over Arctic sea ice: effects](#)
772 [on sea ice thermodynamics and evolution, *The Cryosphere*, 13, 1661-1679, 2019.](#)

773 Yoo, C., Feldstein, S., and Lee, S.: The impact of the Madden–Julian oscillation trend on the Arctic
774 amplification of surface air temperature during the 1979–2008 boreal winter, *Geophys. Res.*
775 *Lett.*, 38, L24804, doi:10.1029/2011GL049881, 2011.

776 Yu, L., Zhong, S., Winkler, J. A., Zhou, M., Lenschow, D. H., Li, B., Wang, X., and Yang, Q.: Possible
777 connections of the opposite trends in Arctic and Antarctic sea-ice cover, *Scientific Reports*, 7,
778 45804, doi:10.1038/srep45804, 2017.

779

780

781

782 Table 1. Spatial correlations (Corrs) between the daily winter (DJF) surface air
 783 temperature and the corresponding SOM pattern for each day from 1979 to 2018.

	3×1	2×2	3×2	4×2	3×3	5×2	4×3	5×3	4×4
Corr	0.26	0.43	0.48	0.48	0.50	0.49	0.50	0.51	0.51

784

785

786

787

788

789

790

791

792

793

794

795

796

797

798

799

800

801

802

803

804

805

806

807

808

809

810

811

812

813

814 Table 2. Averaged anomalous NAO and AO indices for all occurrences of each SOM
 815 node. Asterisks indicate the above 95% confidence level.

816

	Node1	Node2	Node3	Node4	Node5	Node6	Node7	Node8	Node9
NAO	0.38*	0.22*	0.12*	0.05	-0.22*	-0.02	-0.07	-0.31*	-0.32*
AO	0.44*	0.38*	1.03*	-0.42	-0.62*	0.22*	-0.44*	-1.11*	-0.41*

817

818

819

820

821

822

823

824

825

826

827

828

829

830

831

832

833

834

835

836

837

838

839

840

841

842

843

844

845

846

847

848

849

850

851

852

853

854

855 Table 3. Trends in the frequency of occurrences for each SOM node (day yr⁻¹).
856 Asterisks indicate the above 95% confidence level.

857

	Node1	Node2	Node3	Node4	Node5	Node6	Node7	Node8	Node9
Trend	0.80*	0.10	-0.18	0.22*	-0.02	-0.39*	0.17	-0.17	-0.50*

858

859

860

861

862

863

864

865

866

867

868

869

870

871

872

873

874

875

876

877

878

879

880

881

882

883

884

885

886

887

888

889

890

891

892

893

894

895 Table 4. Frequencies of occurrence (%) of wintertime surface air temperature patterns
 896 in Figure 1 for all winters before 1998 and after 1998 for the period 1979-2019.
 897 Values with Asterisks are significantly different from climatology above the 95%
 898 confidence level.

SOM patterns	Frequencies of occurrence		
	All winters	Winters before 1998	Winters after 1998
Node 1	17.1	7.4*	26.8
Node 2	4.4	3.3	5.4
Node 3	17.2	18.8	15.6
Node 4	8.6	5.4	11.7
Node 5	3.4	3.4	3.5
Node 6	10.2	15.2*	2.1*
Node 7	13.7	10.6	16.8
Node 8	10.1	12.1	8.0
Node 9	15.4	23.7*	7.1*

900
 901
 902
 903
 904
 905
 906
 907
 908
 909
 910
 911
 912
 913
 914
 915
 916
 917
 918
 919
 920
 921
 922
 923
 924
 925
 926

927 **Figure Captions**

928 Figure 1. Spatial patterns of SOM nodes for daily wintertime (December, January, and
929 February) surface air temperature anomalies ($^{\circ}\text{C}$) without removing their linear trends
930 from ERA-Interim reanalysis over the 1979-2019 period. The number in brackets
931 denotes the frequency of the occurrence for each node.

932 Figure 2. Corresponding 500-hPa geopotential height anomalies (gpm) without
933 removing their linear trends from ERA-Interim reanalysis over the 1979-2019 period
934 for each node in Figure 1. Dotted regions indicate the above 95% confidence level.
935 The thick black lines show the study region.

936 Figure 3. Corresponding anomalous 850-hPa wind field (ms^{-1}) without removing ~~the~~
937 its linear trend from ERA-Interim reanalysis over the 1979-2019 period for each node
938 in Figure 1. Shaded regions indicate the above 95% confidence level. The thick black
939 lines show the study region.

940 Figure 4. Corresponding anomalous daily accumulated downward longwave radiation
941 (105 W m^{-2}) without removing ~~the~~ its linear trend from ERA-Interim reanalysis over
942 the 1979-2019 period for each node in Figure 1. Dotted regions indicate the above 95%
943 confidence level. The thick black lines denote show the study region.

944 Figure 5. Corresponding anomalous daily accumulated turbulent heat flux (sensible
945 and latent heat) (10^5 W m^{-2}) without removing their linear trends from ERA-Interim
946 reanalysis over the 1979-2019 period for each node in Figure 1. Positive values
947 denote heat flux from atmosphere to ocean and vice versa. Dotted regions indicate the
948 above 95% confidence level. The thick black lines denote show the study region.

949 Figure 6. Corresponding anomalous wintertime sea ice concentration without
950 removing ~~the-its linear~~ trend from the NSIDC over the 1979-2019 period for each
951 node in Figure 1. Dotted regions indicate the above 95% confidence level.

952 Figure 7. Time series of the number of days for occurrence of each SOM node in
953 Figure 1 over the 1979-2019 period. The thick lines denote the trend in time series.

954 Figure 8. Total (top), SOM-explained (middle), and residual (bottom) trend in
955 wintertime (DJF) surface air temperature ($^{\circ}\text{C yr}^{-1}$) over the 1979-2019 period. Dots in
956 the top panel indicate above 95% confidence level.

957 Figure 9. Trends in surface air temperature explained by each SOM node ($^{\circ}\text{C yr}^{-1}$)
958 over the 1979-2019 period. The percentage in the upper of each panel indicates the
959 fraction of the total trend represented by each node.

960 Figure 10. Anomalous SST ($^{\circ}\text{C}$) regressed into the normalized time series of
961 occurrence number for nodes 1, 4, 6, and 9 without removing ~~the-its linear~~ trend from
962 the NOAA over the 1979-2019 period.

963 Figure 11. Anomalous 500-hPa geopotential height (gpm) regressed into the
964 normalized time series of occurrence number for nodes 1, 4, 6, and 9 without
965 removing ~~the-its linear~~ trend from ERA-Interim reanalysis over the 1979-2019 period.

966 Figure 12. The anomalous wave activity flux (vectors) (Takaya and Nakamura, 2001)
967 and stream function (colors, units: $10^7 \text{ m}^2 \text{ s}^{-1}$) regressed onto the normalized time
968 series of occurrence number for nodes 1, 4, 6, and 9 without removing ~~the-their linear~~
969 trends from ERA-Interim reanalysis over the 1979-2019 period.

970 Figure 13. Spatial patterns of SOM nodes for detrended daily wintertime (December,

971 January, and February) surface air temperature anomalies ($^{\circ}\text{C}$) from the 20CR
972 reanalysis for the 1851-2014 period. The number in brackets denotes the frequency of
973 the occurrence for each node.

974 Figure 14. Time series of the number of days for occurrence of each SOM node in
975 Figure 13 from the 20CR reanalysis for the 1851-2014 period. The thick red lines
976 denote the result in Figure 7 from the ERA-Interim reanalysis for the 1979-2019
977 period.

978 Figure 15. The (a) leading pattern and (b) its time series (PC1 and PC2) of EOF
979 analysis of wintertime surface air temperature anomalies from the 20CR reanalysis for
980 the 1851-2014 period. Prior to EOF analysis, surface air temperature data are
981 detrended. A 40-yr low-pass filter is applied to the time series of PC1, PC2, AMO,
982 PDO, and central North Pacific Ocean (CNPO) indices. The correlation coefficients
983 between PC1 and AMO, PDO and CNPO indices are -0.46 ($p < 0.0001$), 0.38
984 ($p < 0.0001$), and -0.19 ($p = 0.019$); those between PC2 and AMO, PDO and CNPO
985 indices are -0.44 ($p < 0.0001$), 0.38 ($p < 0.0001$), and -0.26 ($p = 0.0009$).

986

987

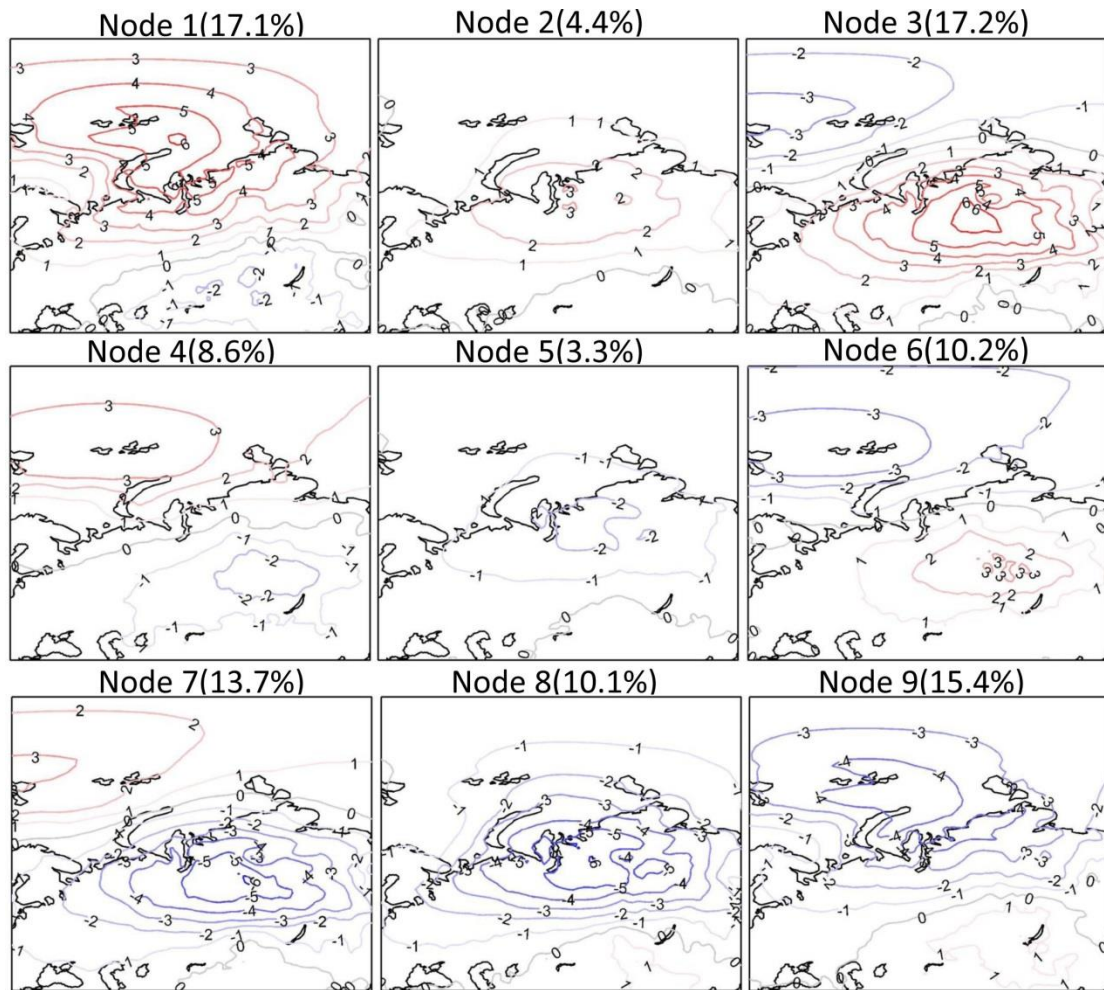
988

989

990

991

992



994

995 Figure 1. Spatial patterns of SOM nodes for daily wintertime (December, January, and February)
 996 surface air temperature anomalies (°C) without removing their linear trends from ERA-Interim
 997 reanalysis over the 1979-2019 period. The number in brackets denotes the frequency of the
 998 occurrence for each node.

999

1000

1001

1002

1003

1004

1005

1006

1007

1008

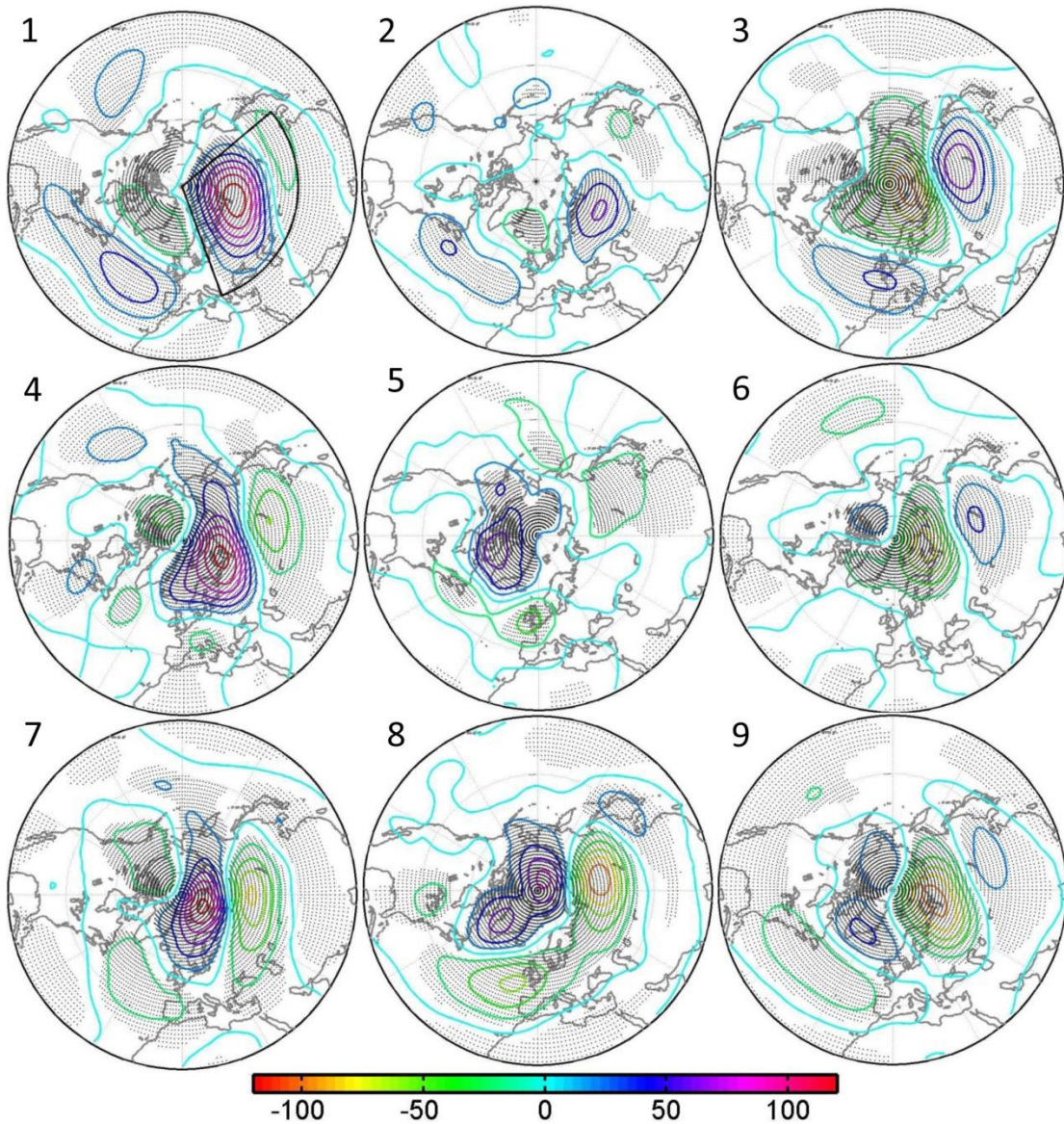
1009

1010

1011

1012

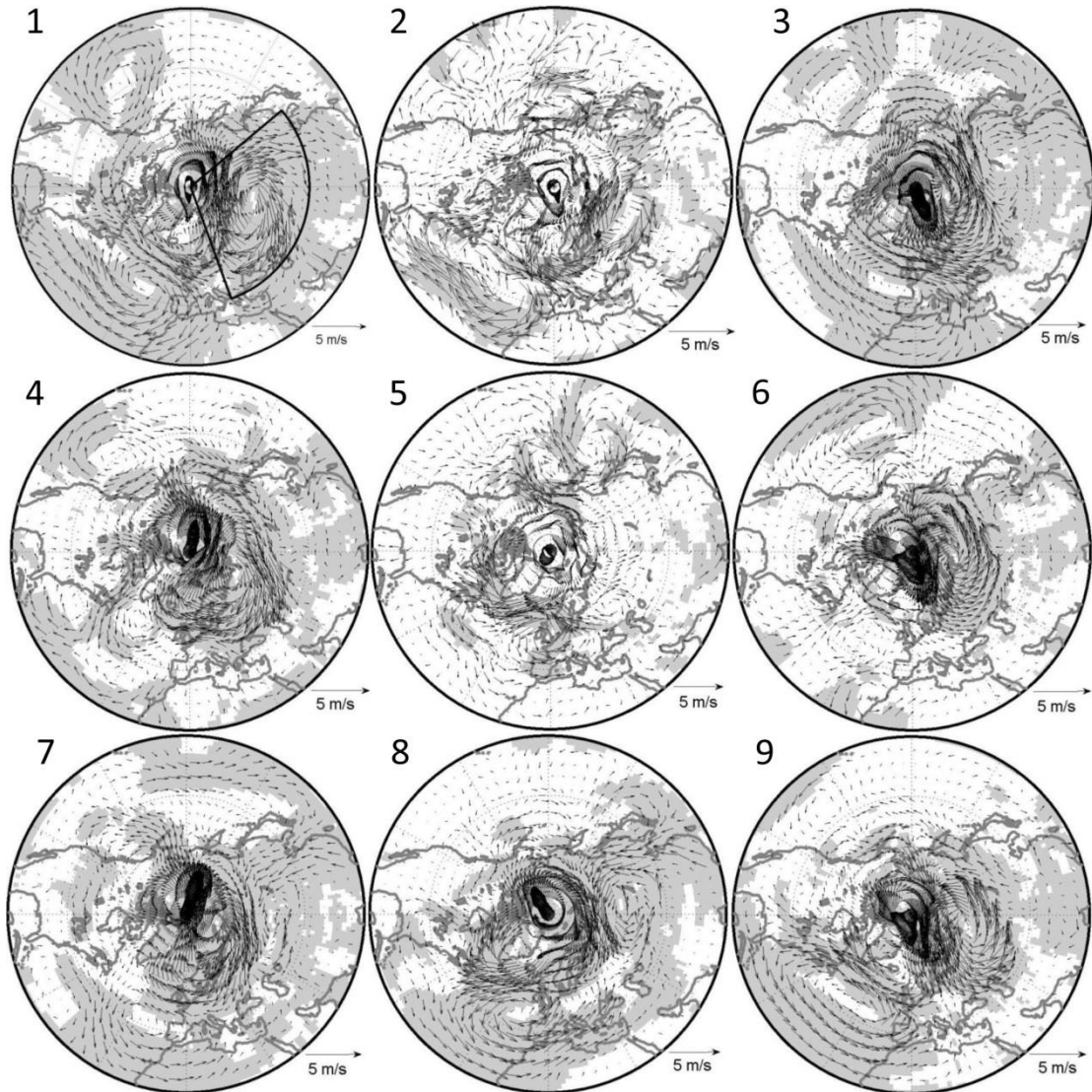
1013



1015
 1016
 1017
 1018
 1019
 1020
 1021
 1022
 1023
 1024
 1025
 1026
 1027
 1028
 1029
 1030

Figure 2. Corresponding 500-hPa geopotential height anomalies (gpm) without removing their linear trends from ERA-Interim reanalysis over the 1979-2019 period for each node in Figure 1. Dotted regions indicate the above 95% confidence level. The thick black lines denote-show the study region.

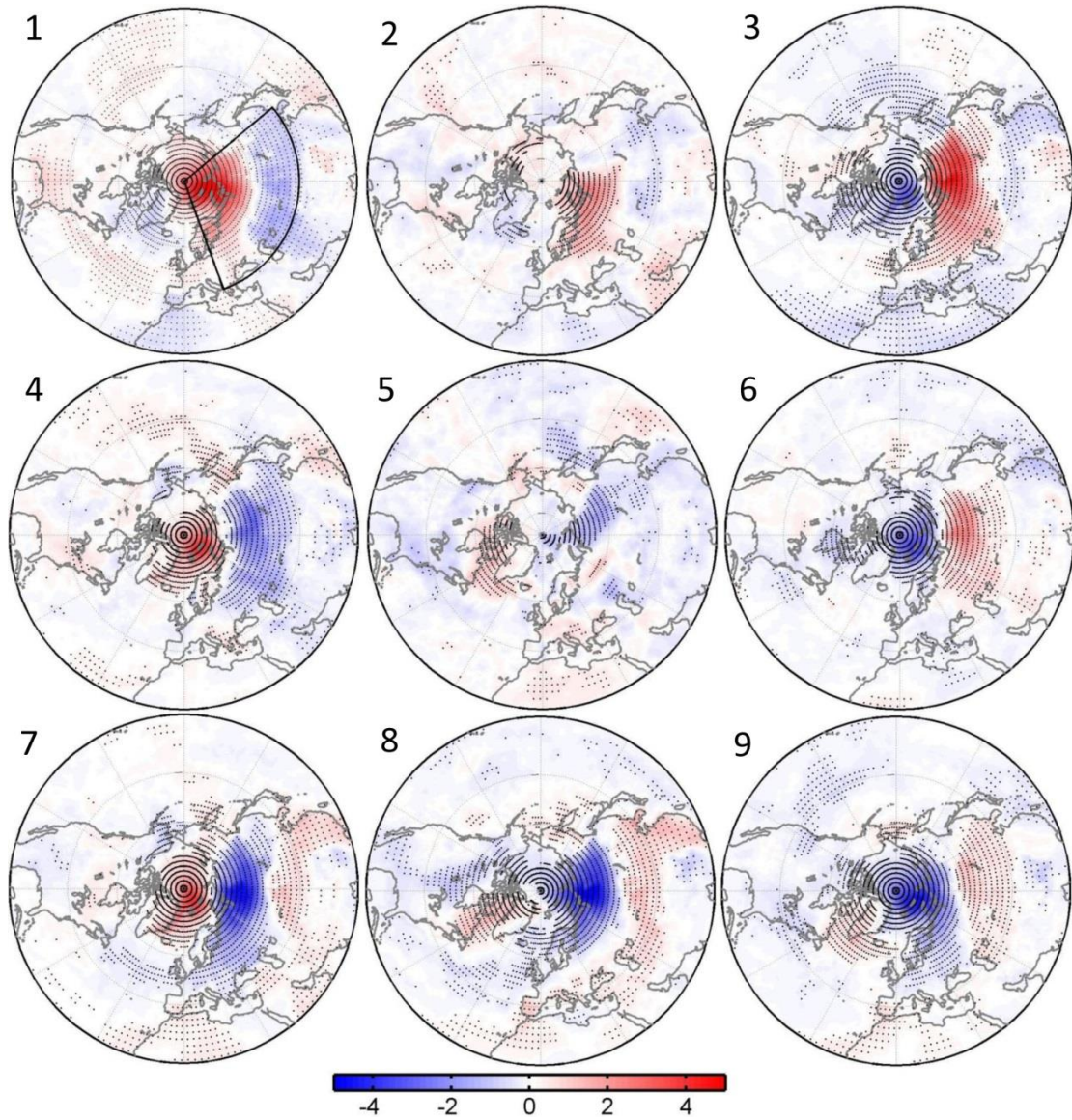
1031
1032
1033



1034
1035
1036
1037
1038
1039
1040
1041
1042
1043
1044
1045
1046
1047
1048

Figure 3. Corresponding anomalous 850-hPa wind field ~~(ms^{-1})~~ without removing its linear trend from ERA-Interim reanalysis over the 1979-2019 period for each node in Figure 1. Shaded regions indicate the above 95% confidence level. The thick black lines ~~denotes~~ show the study region.

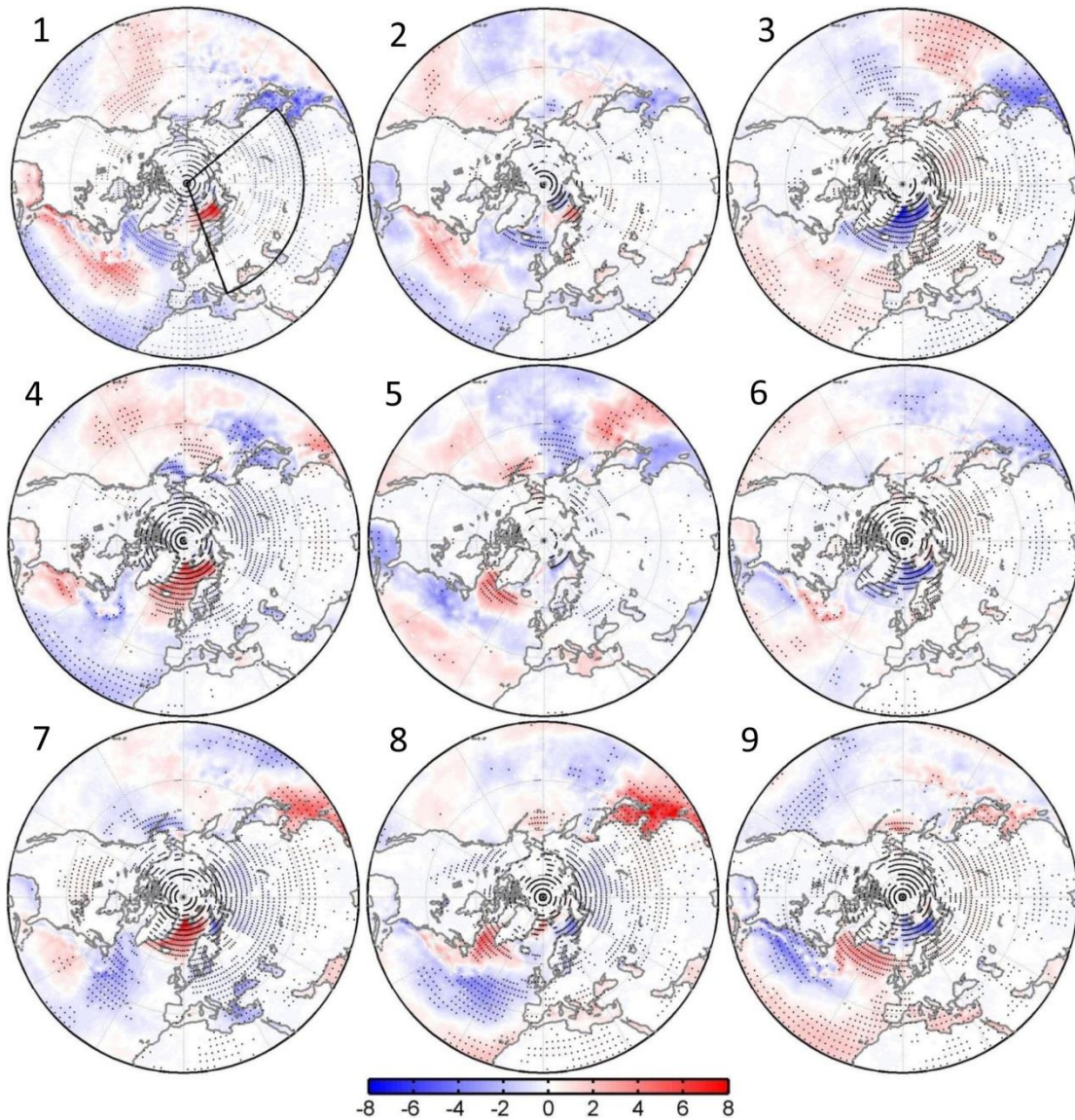
1049
1050
1051
1052
1053
1054



1055
1056
1057
1058
1059
1060
1061
1062
1063
1064
1065

Figure 4. Corresponding anomalous daily accumulated downward longwave radiation (10^5 W m^{-2}) without removing its linear trend from ERA-Interim reanalysis over the 1979-2019 period for each node in Figure 1. Dotted regions indicate the above 95% confidence level. The thick black lines denote-show the study region.

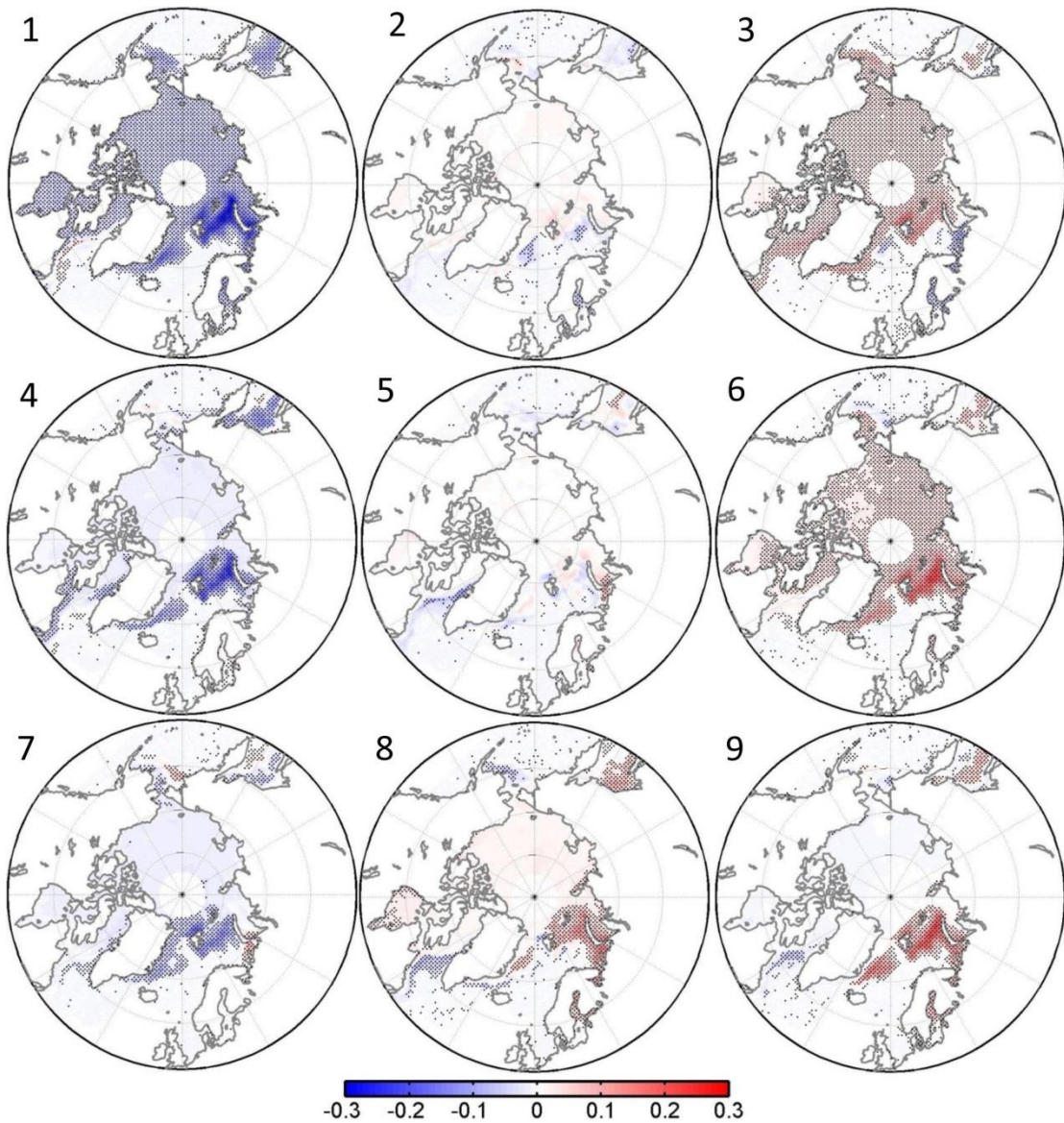
1066
1067
1068
1069
1070
1071
1072
1073
1074



1075
1076
1077
1078
1079
1080
1081
1082

Figure 5. Corresponding anomalous daily accumulated turbulent heat flux (sensible and latent heat) (10^5 W m^{-2}) without removing their linear trends from ERA-Interim reanalysis over the 1979-2019 period for each node in Figure 1. Positive values denote heat flux from atmosphere to ocean and vice versa. Dotted regions indicate the above 95% confidence level. The thick black lines denote show the study region.

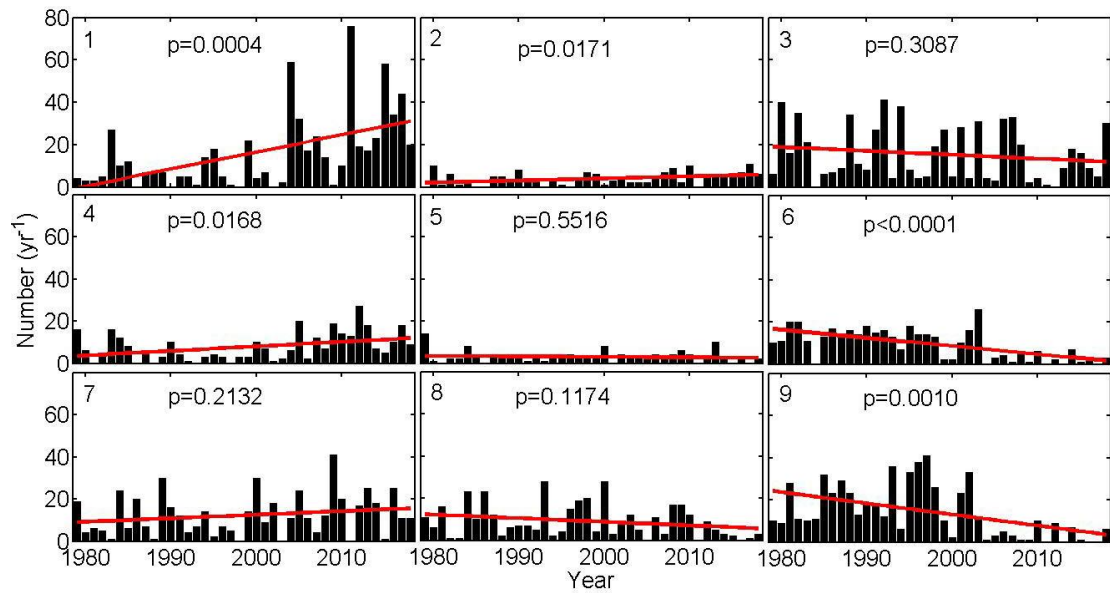
1083
1084
1085
1086
1087
1088
1089
1090
1091
1092
1093
1094



1095
1096
1097
1098
1099

Figure 6. Corresponding anomalous wintertime sea ice concentration without removing its linear trend from the NSIDC over the 1979-2019 period for each node in Figure 1. Dotted regions indicate the above 95% confidence level.

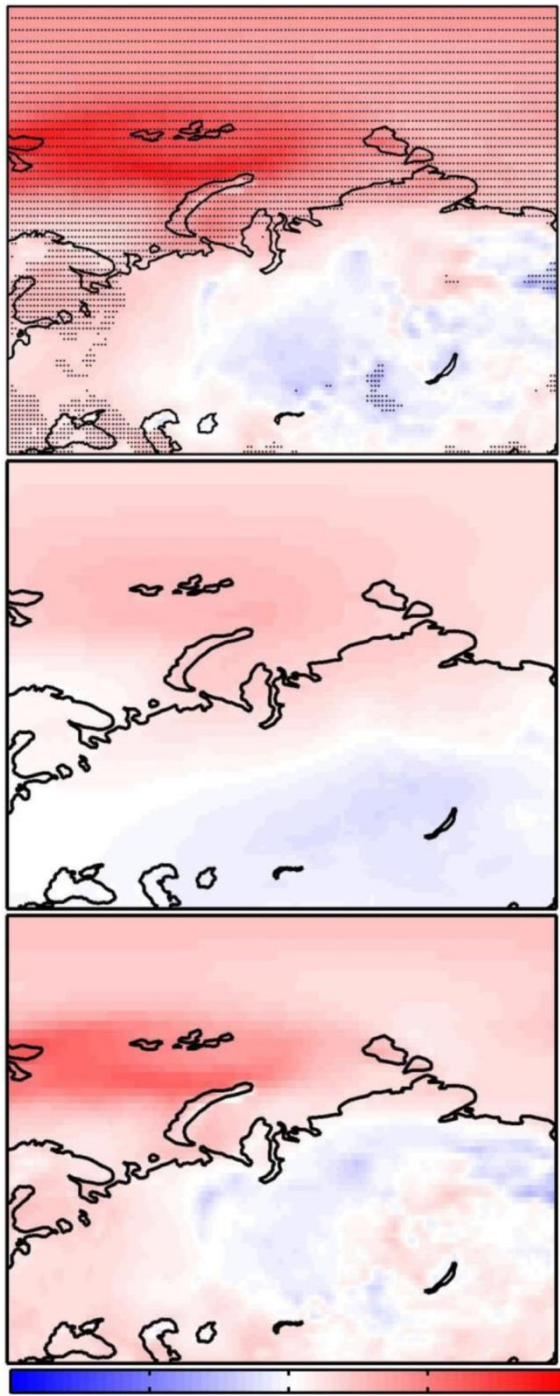
1100
1101
1102
1103
1104
1105
1106
1107
1108
1109
1110
1111
1112
1113
1114



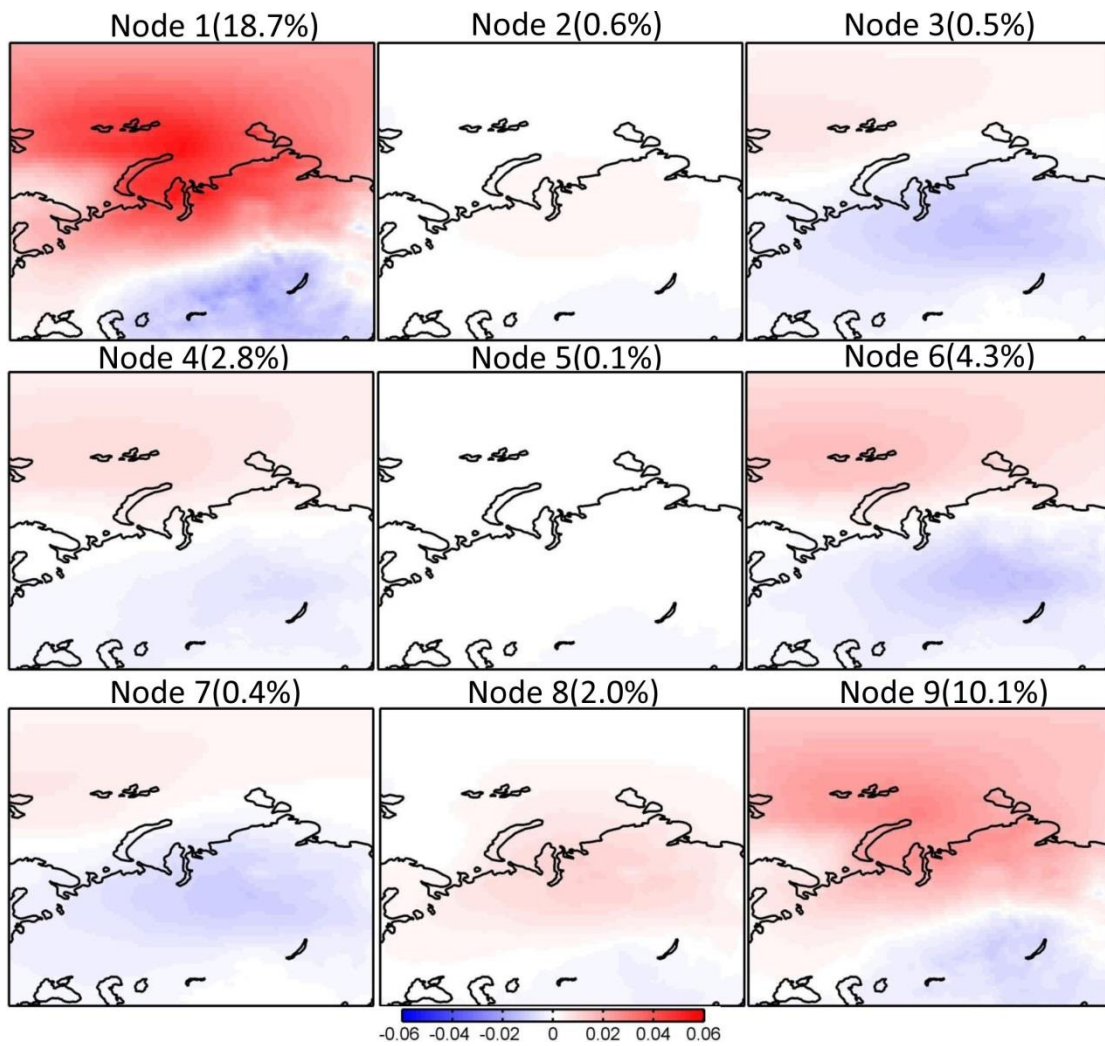
1115
1116
1117
1118
1119
1120
1121
1122
1123
1124
1125
1126
1127
1128
1129

Figure 7. Time series of the number of days for occurrence of each SOM node in Figure 1 over the 1979-2019 period. The thick lines denote the trend in time series.

1130
1131
1132



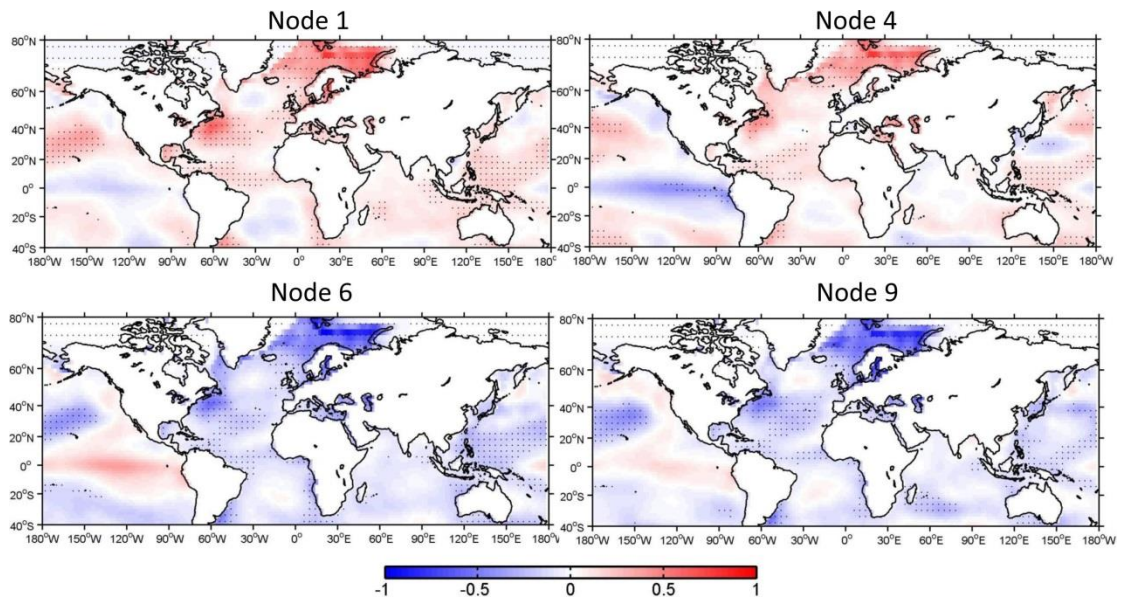
1133 -0.4 -0.2 0 0.2 0.4
1134 Figure 8. Total (top), SOM-explained (middle), and residual (bottom) trend in wintertime (DJF)
1135 | surface air temperature ($^{\circ}\text{C yr}^{-1}$) over the 1979-2019 period. Dots in the top panel indicate above
1136 | 95% confidence level.
1137



1138
1139
1140
1141
1142
1143
1144
1145
1146
1147
1148
1149
1150
1151
1152
1153
1154
1155
1156
1157

Figure 9. Trends in surface air temperature explained by each SOM node ($^{\circ}\text{C yr}^{-1}$) over the 1979-2019 period. The percentage in the upper of each panel indicates the fraction of the total trend represented by each node.

1158
1159



1160

1161 Figure 10. Anomalous SST ($^{\circ}\text{C}$) regressed into the normalized time series of occurrence number
1162 for nodes 1, 4, 6, and 9 without removing its linear trend from the NOAA over the 1979-2019
1163 period.

1164

1165

1166

1167

1168

1169

1170

1171

1172

1173

1174

1175

1176

1177

1178

1179

1180

1181

1182

1183

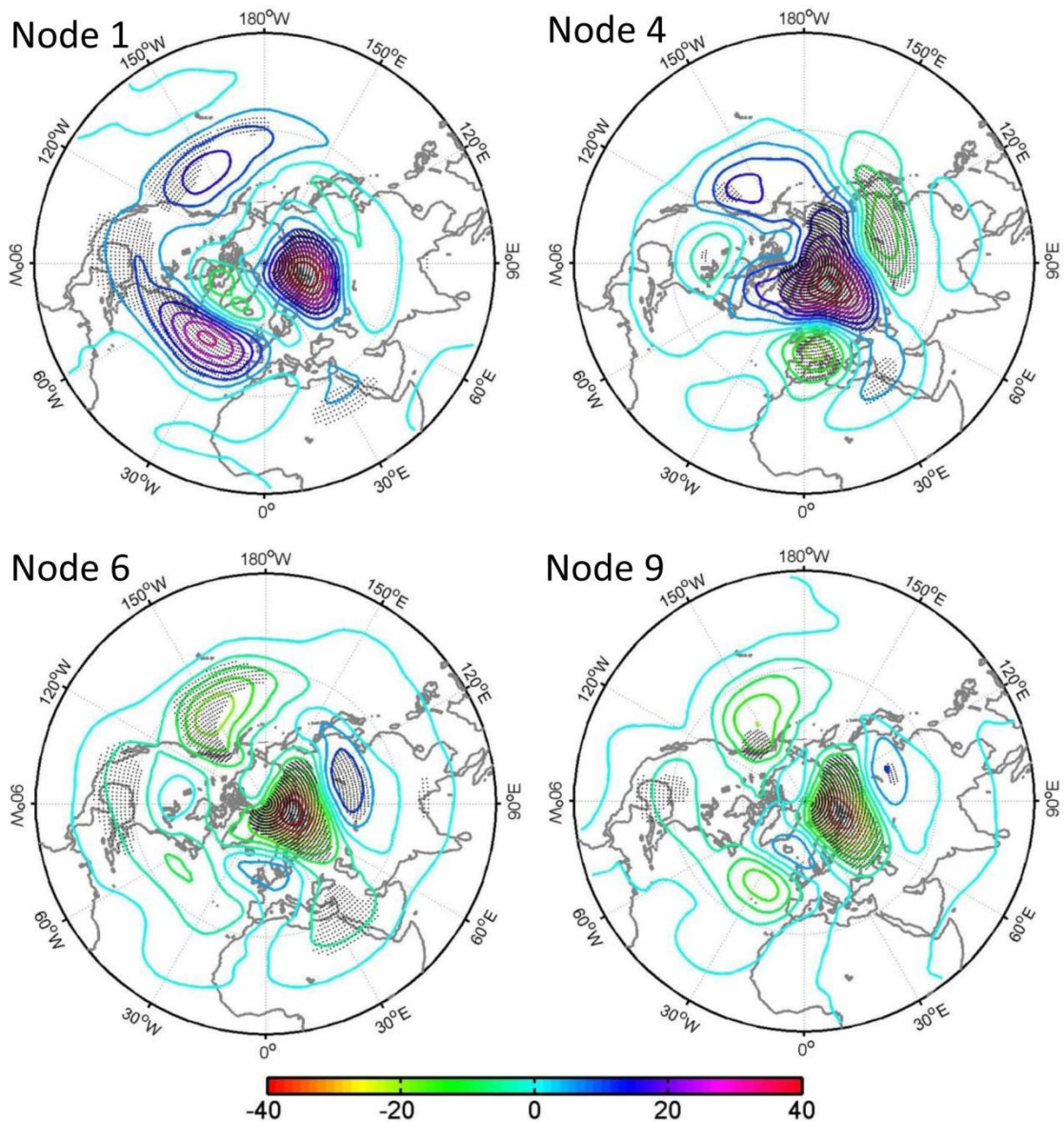
1184

1185

1186

1187

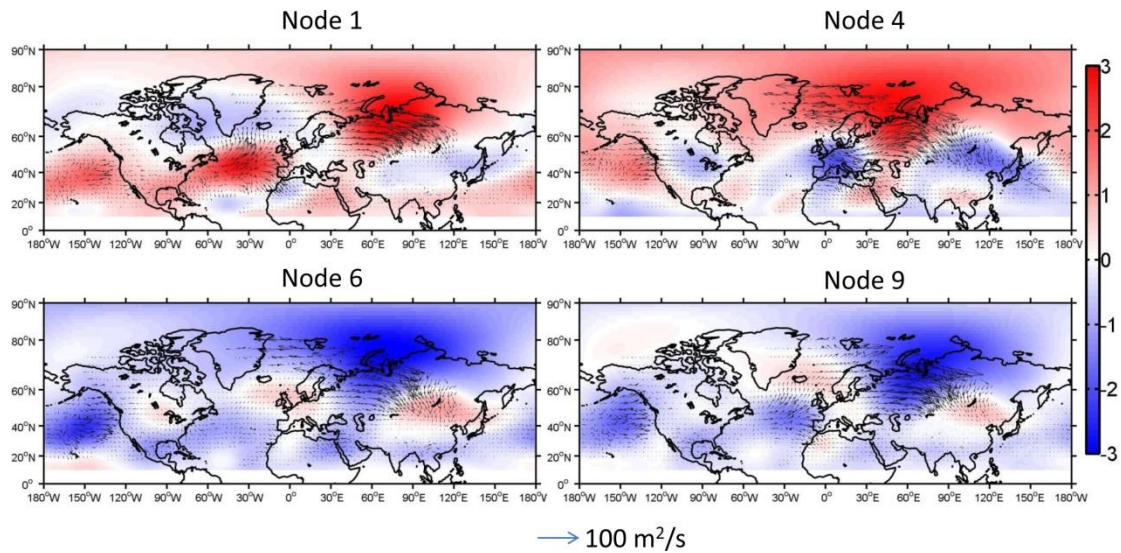
1188
1189
1190
1191



1192
1193
1194
1195
1196
1197
1198
1199
1200
1201
1202
1203

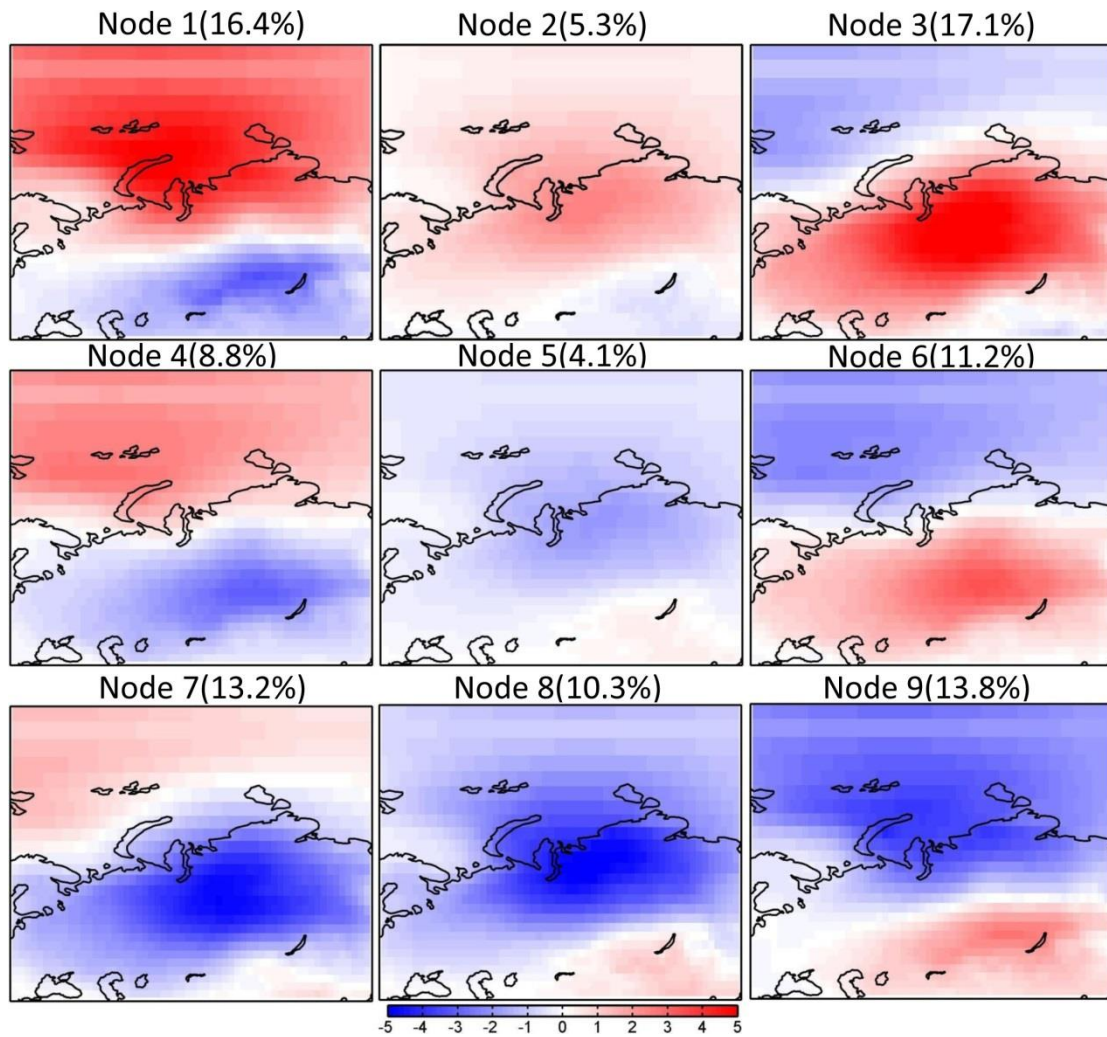
Figure 11. Anomalous 500-hPa geopotential height (gpm) regressed into the normalized time series of occurrence number for nodes 1, 4, 6, and 9 without removing its linear trend from ERA-Interim reanalysis over the 1979-2019 period.

1204
1205
1206
1207
1208



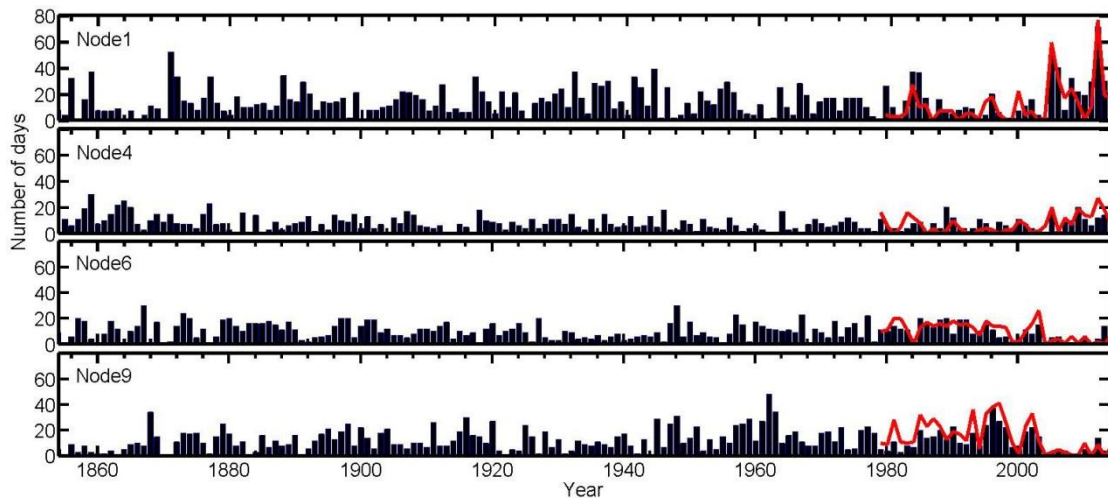
1209
1210
1211
1212
1213
1214
1215
1216
1217
1218
1219
1220
1221
1222

Figure 12. The anomalous wave activity flux (vectors) (Takaya and Nakamura, 2001) and stream function (colors, units: $10^7 \text{ m}^2/\text{s}^{-1}$) regressed onto the normalized time series of occurrence number for nodes 1, 4, 6, and 9 without removing their linear trends from ERA-Interim reanalysis over the 1979-2019 period.



1223
1224
1225
1226
1227
1228
1229
1230
1231
1232
1233
1234
1235
1236
1237
1238
1239
1240
1241
1242
1243

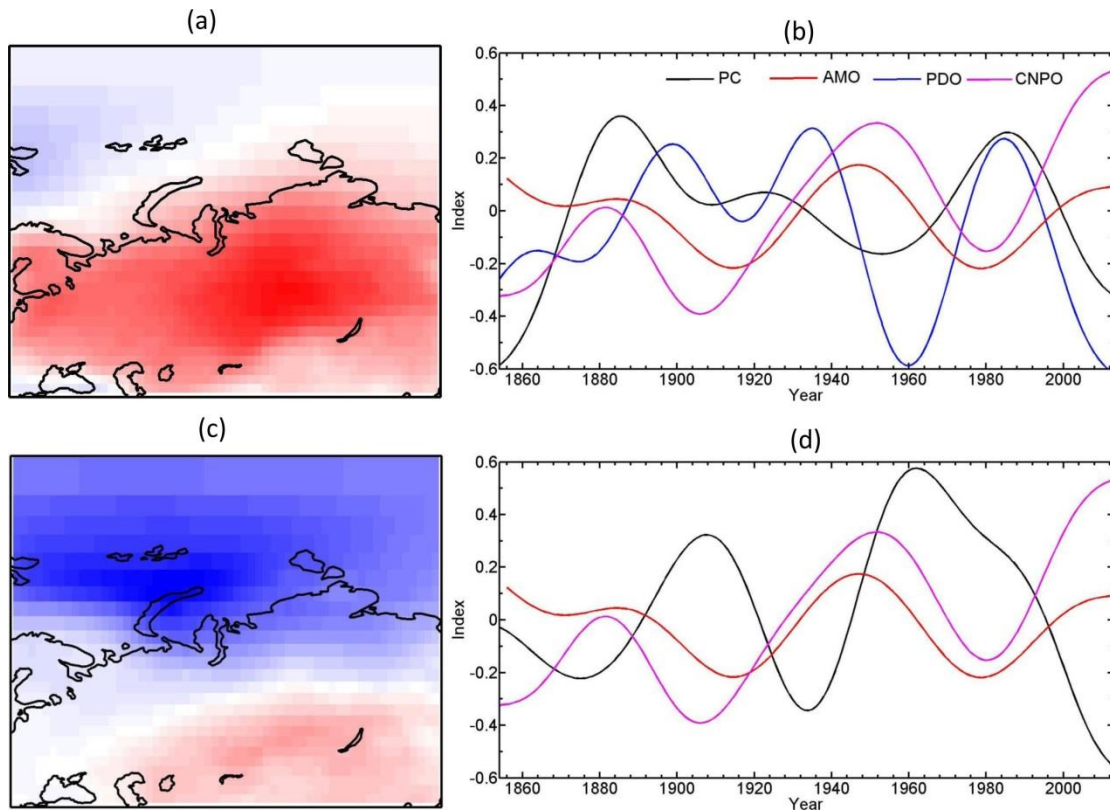
Figure 13. Spatial patterns of SOM nodes for detrended daily wintertime (December, January, and February) surface air temperature anomalies (°C) from the 20CR reanalysis for the 1851-2014 period. The number in brackets denotes the frequency of the occurrence for each node.



1244
 1245
 1246
 1247
 1248
 1249
 1250
 1251
 1252
 1253
 1254
 1255
 1256
 1257
 1258
 1259
 1260
 1261
 1262
 1263
 1264
 1265
 1266
 1267
 1268
 1269
 1270
 1271
 1272
 1273
 1274
 1275
 1276

Figure 14. Time series of the number of days for occurrence of each SOM node in Figure 13 from the 20CR reanalysis for the 1851-2014 period. The thick red lines denote the result in Figure 7 from the ERA-Interim reanalysis for the 1979-2019 period.

1277
1278



1279

1280 Figure 15. The (a) leading pattern and (b) its time series (PC1 and PC2) of EOF analysis of
1281 wintertime surface air temperature anomalies [from the 20CR reanalysis for the 1851-2014 period.](#)
1282 Prior to EOF analysis, surface air temperature data are detrended. A 40-yr low-pass filter is
1283 applied to the time series of PC1, PC2, AMO, PDO, and central North Pacific Ocean (CNPO)
1284 indices. The correlation coefficients between PC1 and AMO, PDO and CNPO indices are -0.46
1285 ($p < 0.0001$), 0.38 ($p < 0.0001$), and -0.19 ($p = 0.019$); those between PC2 and AMO, PDO and
1286 CNPO indices are -0.44 ($p < 0.0001$), 0.38 ($p < 0.0001$), and -0.26 ($p = 0.0009$).

1287